Noise From Shallow Underwater Explosions

Alexander G. Soloway

Thesis submitted for partial requirement of degree program for

Master of Science in Mechanical Engineering

University of Washington

2014

Thesis Committee

Peter H. Dahl, Chair

Robert Odom

Michael Bailey

Program Authorized to Offer Degree:
Mechanical Engineering

University of Washington

Abstract

Noise From Shallow Underwater Explosions

Alexander G. Soloway

Chair of the Supervisory Committee:
Professor Peter H. Dahl
Mechanical Engineering

Naval activities such as ordnance disposal, demolition and requisite training, can involve detonation of small explosive charges in shallow water that have the potential to harm nearby marine life. Measurements of the underwater sound generated by sub-surface explosions were collected as part of a naval training exercise. In this thesis the noise levels from these explosions will be investigated using peak pressure, sound exposure level and energy spectral density. Measurements of very-low frequeny Scholte interface waves will also be presented and used to investigate elastic parameters in the sediment.

ACKNOWLEDGMENTS

I would like to acknowledge and thank a number of people who haved given their help and support as I have completed my degree. First I would like to give my sincere thanks to my advisor, Peter Dahl, for his support that has allowed me to complete this degree and for his genuine passion for underwater acoustics that has rubbed off on me.

I would also like to thank Bob Odom for opening his door to my questions and for providing useful guidance during my journey into the enigmatic world of seismo-acoustics, and Mike Bailey for generously being a part of my thesis committee.

I would like to give a special thanks to Andy Ganse and Brian Dickinson as without their help I would still be working to compile OASES. I would also like to thank my other lab mates, David Dall'Osto, Dara Farrell and Paul Murphy, for all of their help.

Finally I would like to give my thanks to my family for their love and support, and for helping me to see the importance of doing what makes me happy.

DEDICATION

To my family for their unconditional love and support and their infinite patience

TABLE OF CONTENTS

LIST OF FIGURES

Chapter 1

INTRODUCTION

Naval activities such as ordnance disposal, demolition and requisite training, can involve detonation of small explosive charges in shallow water. On 11 September, 2012 a team from the University of Washington, along with personnel from Naval Engineering Facilities Command Atlantic (NAVFAC-LANT), and HDR Inc. conducted a set of measurements of the underwater sound generated by sub-surface explosions from a training exercise for a navy ordnance disposal team off the coast of Virginia Beach, Virginia.

This work presents these underwater sound measurements with focus on peak pressures, sound exposure levels (SEL) and time-series analysis. Additionally, the influences of elastic properties in the seabed are investigated. The goals of this work are to provide both accurate ground-truth data and improved modeling of such sound, so as to ultimately reduce potential impacts on marine life.

The thesis is organized as follows. Chapter 2 presents a brief overview of underwater explosion research including semi-empirical equations for peak pressure from explosions and the calculation of the sound exposure level. Chapter 3 gives a discussion on a normal mode solution for the sound field in a simple fluid-solid environment. Chapter 4 summarizes the Virginia Beach measurements. In Chapter 5 experimental results for the peak pressure, bubble pulse period and SEL are presented. Also included here are results from the application of auditory weighting functions for marine mammals and sea turtles as well as a discussion on elastic effects and measurements of Scholte interface waves. A summary is given in Chapter 6.

Chapter 2

BACKGROUND

Chapman [1] provided a relatively recent review and discussion of the general characteristics of underwater explosions. He explains that during the detonation of an underwater charge, the explosive material is transformed into a small sphere of gas at high temperature and pressure. As a result of the pressure difference between the gas sphere and the hydrostatic pressure in the water, a shock wave is radiated into the water. Following detonation the gas sphere begins to expand outward resulting in a pressure tail behind the shock wave that exponentially decreases in magnitude. As the bubble expands the pressure inside begins to decrease. When the pressure inside the bubble reaches the hydrostatic pressure of the water, the inertia of the moving gas causes the bubble to continue to expand. This continued expansion of the gas results in the pressure within the gas sphere falling below the hydrostatic pressure. Eventually the gas sphere ceases to expand. With the pressure inside the gas sphere now below the hydrostatic pressure, the bubble begins to contract thereby increasing the internal pressure. Similar to the expansion process, the inertia of the gas bubble causes the pressure within the sphere to increase past the hydrostatic pressure. This process of expansion and contraction, collectively referred to as the bubble pulse, continues until the energy within the gas sphere has been radiated into the water [1]. A notional pressure history of the explosive waveform as it relates to the size of the gas sphere is shown in Figure 2.1. The time between the shock arrival, P_{peak}, and the peak pressure of the bubble pulse P_1, is referred to as the bubble pulse period, τ.

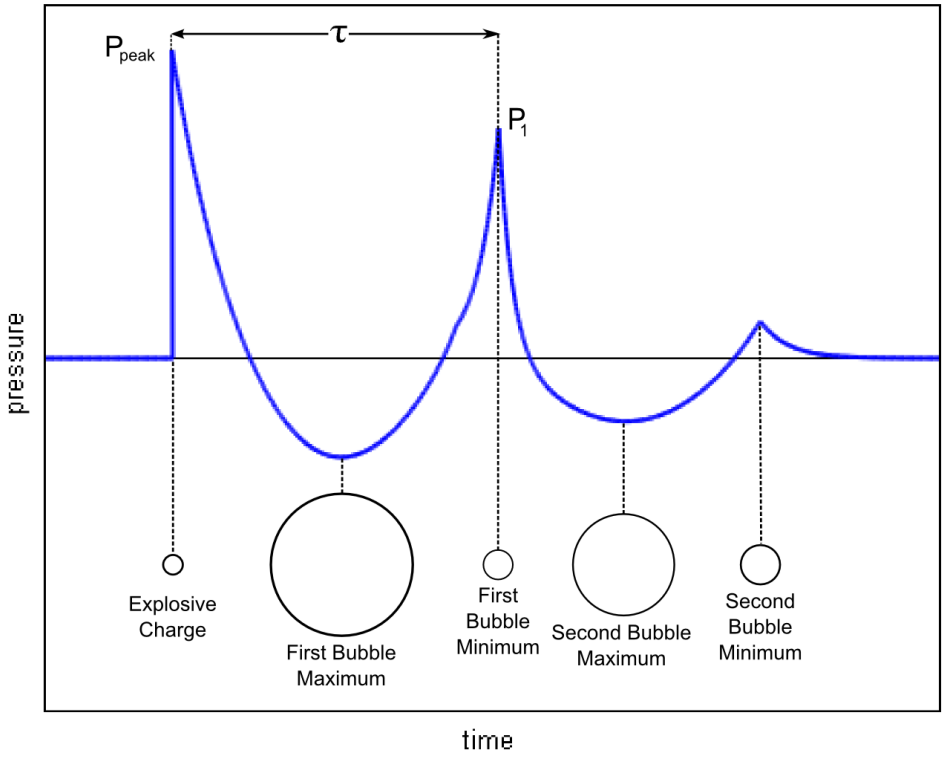

Figure 2.1: Notional pressure-time history for an underwater explosion with the size of the gas sphere shown in relation to the explosion waveform

2.1 Semi-Empirical Equation

In the following section the semi-empirical equations for the peak pressure and energy flux density are presented.

2.1.1 Peak Pressure

Using experimental measurements of underwater explosions collected during and after World War II, a semi-empirical equation for predicting the peak pressure from underwater explosions was developed as a function of the scaling parameter $R/W^{1/3}$, defined as the range from the source, R, divided by charge weight, W, to the one-third power (herein referred

to as scaled range.) The term semi-empirical has been used to describe this peak pressure equation due to the origins of this parameter in Kirkwood-Bethe propagation theory [2]. The peak pressure is given by [3]

$$P_{peak} = 52.4 \times 10^6 \left(\frac{W^{1/3}}{R} \right)^{1.13} \tag{2.1}$$

where P_{peak} is the peak pressure in Pascal (Pa), R the measurement range in meters (m), and W the charge weight in kilograms of TNT (kg-TNT). It is important to note that this equation was developed for TNT, due to its historical and continued use as the standard high explosive, and assumes a spherical TNT charge of density 1520 kg/m^3 [4]. Using this equation, the peak pressure for other high explosives can be predicted through the use of TNT-equivalent weight. While originally formulated for spherical charges, the equation has been successfully employed for a wide array of charge geometries [1, 5–7].

While a full derivation of the Kirkwood-Bethe theory is outside the scope of this thesis, it has been shown that the pressure in the water decays exponentially with time, and is dependent only on the explosive material and the ratio of the range to the charge radius, R/a_o [4]. The peak-pressure equation assumes a spherical charge geometry where the charge weight is given by $W = \rho\frac{4}{3}\pi a_o^3$ where ρ denotes the density of the explosive material. With this in mind, the ratio R/a_o can be reformulated as

$$\frac{R}{a_o} = \frac{R}{W^{1/3}} \times \left(\rho\frac{4}{3}\pi \right)^{1/3} \tag{2.2}$$

In the peak pressure equation $\left(\rho\frac{4}{3}\pi\right)^{1/3}$ is absorbed into the 52.4×10^6 factor. Additionally, the Kirkwood-Bethe theory supports the $R^{-1.13}$ decay of the peak pressure with range, which is a somewhat greater decay rate than the R^{-1} decay expected for spherical spreading of an acoustic wave [4].

2.1.2 Energy Flux Density

The energy flux density, E is defined as the time integral of the squared acoustic pressure divided by the product of the sound speed, c, and density, ρ, of the medium, or

$$E = \frac{1}{c\rho} \int_0^\infty p^2(t) dt \tag{2.3}$$

The pressure signature from an underwater explosion can be modelled as decaying exponentially with time, t

$$P(t) = P_{peak} e^{-t/\theta} \tag{2.4}$$

with a decay constant θ given by

$$\theta = 9.25 \times 10^{-5} W^{1/3} \left(\frac{R}{W^{1/3}} \right)^{0.14} \tag{2.5}$$

where θ is in seconds [1].

A semi-empirical equation for the energy flux density can be found by combining Equations 2.4 and 2.5 in Equation 2.3

$$\begin{aligned} E &= \frac{1}{\rho\, c} \int_0^\infty \left(P_{peak} e^{-t/\theta} \right)^2 dt \\ &= \frac{1}{\rho\, c} (52.4 \times 10^6)^2 \left[\left(\frac{W^{1/3}}{R} \right)^{1.13} \right]^2 \int_0^\infty e^{-2t/\theta} dt \\ &= \left(\frac{2.75 \times 10^{15}}{\rho\, c} \right) \left(\frac{W^{1/3}}{R} \right)^{2.26} \left(\frac{-\theta}{2} \right) e^{-2t/\theta} \Big|_{t=0}^{\infty} \\ &= \left(\frac{2.75 \times 10^{15}}{\rho\, c} \right) \left(\frac{W^{1/3}}{R} \right)^{2.26} \left(\frac{-9.25 \times 10^{-5}\, W^{1/3} \left(\frac{W^{1/3}}{R} \right)^{-0.14}}{2} \right) \left(e^{-\infty} - e^{0} \right) \end{aligned} \tag{2.6}$$

noting that

$$\lim_{x \to \infty} e^{-x} = 0 \tag{2.7}$$

Equation 2.6 reduces to

$$E = \left(\frac{1.27 \times 10^{11}}{\rho\, c} \right) \left(\frac{W^{1/3}}{R} \right)^{2.26} \left(W^{1/3} \left(\frac{W^{1/3}}{R} \right)^{-0.14} \right) \tag{2.8}$$

Combining the $W^{1/3}/R$ terms and ignoring constant values, it can be shown that

$$E \propto W^{1/3} \left(\frac{W^{1/3}}{R} \right)^{2.12} \tag{2.9}$$

Proportional relations for Equation 2.9 are given by Cole [8], Arons [3], Slifko [9], and Wakeley [5]. These equations differ in the term 2.12 as a result of differences in Equations 2.1 and 2.5. Chapman's results for Equation 2.5 have been used as they were collected in a more study involving high resolution instrumentation.

2.2 Sound Exposure Level

The sound exposure level (SEL) is the time integral of the squared acoustic pressure

$$SEL = 10 \log_{10} \left(\int_0^T p^2(t) dt \right) \tag{2.10}$$

where SEL is in units of dB referenced $1 \mu Pa^2 s$. Popper [10] explains that SEL is an indication of the total acoustic energy received by an organism. It has become a useful metric to assess cumulative noise exposure as it allows for the comparison of sounds with varying durations [11].

One approach to calculating the SEL is the 90% energy approach (SEL_{90}), where the integration period, T, is defined as the sample interval that includes 90% of the energy of the explosions waveform. An example of this calculation is shown below (Figure 2.2). An alternate approach is the 100% energy approach where the integration window, T, includes all of the energy in the received waveform.

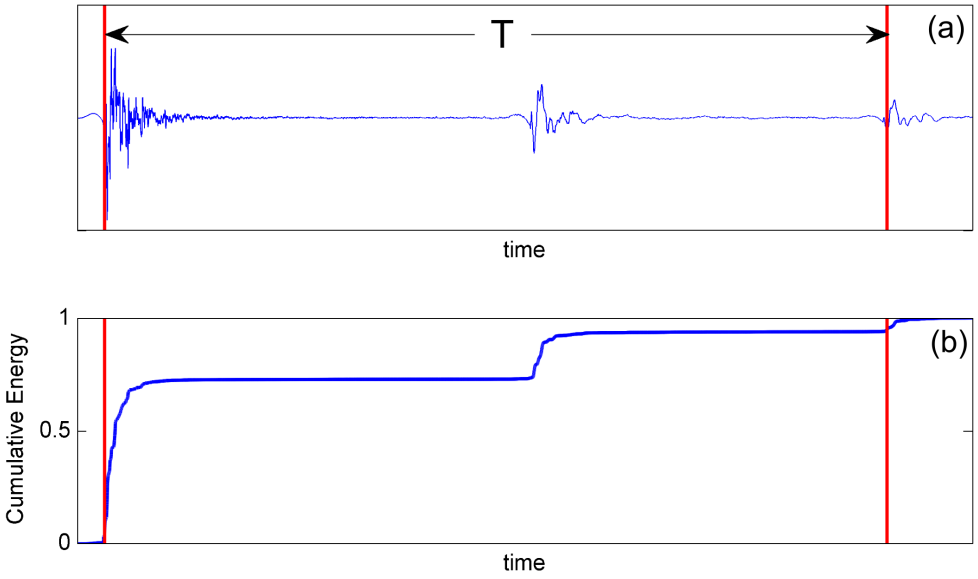

Figure 2.2: a) Time history of an explosion and b) the resulting cumulative energy. The red lines indicate the start and end times of the window containing 90% of the waveform energy.

2.3 Auditory Weighting Functions

Different classes of marine species show variable sensitivity to underwater noise based on differences in their hearing. To emphasize frequencies where sensitivity to this noise is high and de-emphasize frequencies where sensitivity is low, auditory weighting functions are used. Such functions specific to the type of underwater noise studied here are from the report, The Criteria and Thresholds for U.S. Navy Acoustic and Explosive Effects Analysis" [12].

Six functional hearing groups are identified (Table 2.1), one for turtles, and five for marine mammals. All species in a specific group are considered to be equally susceptible to noise. The auditory frequency ranges listed in Table 2.1 should not be confused with auditory weighting functions, as the former serve merely as a guide to the range of auditory reception. Auditory weighting functions (see original report [12]) corresponding to the six functional hearing groups are shown in Figure 2.3. Their interpretation is as follows: Energy

at frequencies for which the weighting is less than 0 dB is discounted or given less weight in an energy metric such as the Sound Exposure Level or SEL, e.g. the auditory weighing function associated with Phocids (e.g. earless seals) and Sirenians (e.g. manatees) calls for such a reduction for frequencies less than about 100 Hz. Additional details on the creation and interpretation of auditory weighting function pertaining to the effects of underwater sound on marine life can be found in Southall et al. [11].

Table 2.1: *Summary of the functional hearing groups and auditory frequency ranges.*

Function Hearing Group	**Sample of Functional Hearing Group Species**	**Auditory Frequency Range (Hz)**
Low-frequency cetacean	Baleen whale, humback whale	7 - 22,000
Mid-frequency Cetaceans	Bottlenose dolphin, killer whale, pilot whale	150 - 160,000
High-frequency Cetaceans	harbor porpoise, river dolphin	200 - 180,000
Phocids Sirenians	earless seal manatees, dugong	75 - 75,000
Otariids Odobenids Mustelids Ursids	eared seal walrus sea otter polar bear	100 - 50,000
Sea Turtles	Loggerhead Turtle	100 - 1,000

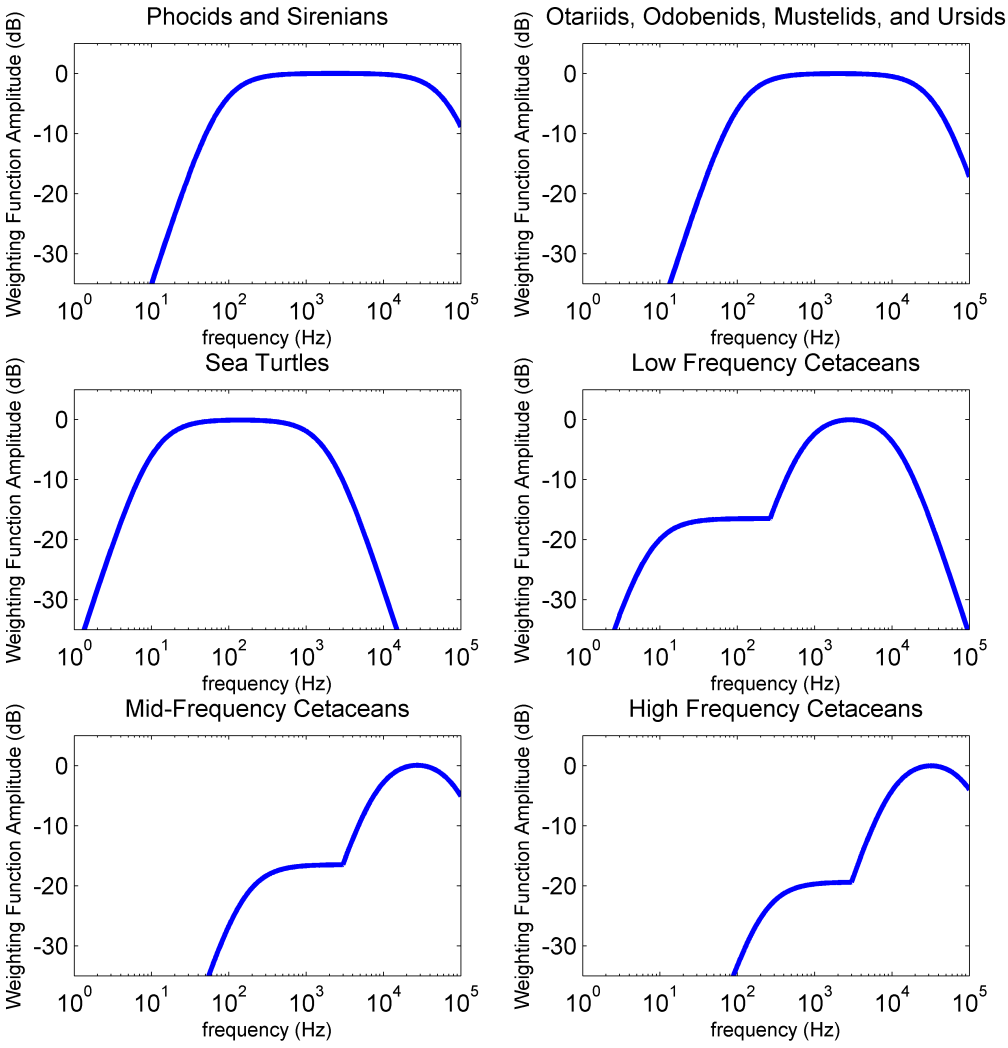

Figure 2.3: Auditory weighting functions corresponding to the six functional hearing groups (Table 1).

2.4 Elastic Parameters in the Sediment

Scholte waves are a type of seismic wave that propagates along the water-seabed interface at a phase speed equal to approximately 90 - 95% of the shear wave speed [13]. The Scholte wave propagates parallel to the seabed and causes a rolling motion in the sediment (Figure

2.4 (a)), while perpendicular to the seabed it decays exponentially with distance away from the interface in both the water and the sediment.

At the water-sediment interface, the Scholte wave has retrograde elliptical particle motion (Figure 2.4 (b)). With increasing depth into the sediment the horizontal component decreases until the particle velocity becomes purely vertical at a distance of approximately one-fifth of the wavelength associated with Scholte wave propagation in the sediment. $\lambda_{scholte}$ given by

$$\lambda_{scholte} = \frac{2\pi}{\beta_{scholte}} \tag{2.11}$$

where $\beta_{scholte}$ is the vertical wave number associated with the Scholte wave, and is given by

$$\beta_{scholte} = 2\pi f \left(\frac{1}{c_{water}^2} - \frac{1}{c_{scholte}^2} \right)^{1/2} \tag{2.12}$$

where c_{water} is the sound speed in the water, and $c_{scholte}$ the phase speed of the Scholte wave [13]. At greater depths the particle motion once again becomes elliptical albeit with pro-grade motion [13]. An example of prograde versus retrograde particle motion as they are defined in this thesis is shown in Figure 2.5. Additionally, the amplitude of the Scholte wave decays to zero within one wavelength from the water-sediment interface. As a result, lower frequencies (with larger wavelengths) penetrate deeper into the sediment [14].

Another important feature is the frequency dependence of the Scholte wave speed, also referred to as dispersion. For a homogeneous medium the Scholte wave is non-dispersive, however real environments typically have complex bottoms with layers, and shear and compressional wave speed gradients that increase with depth. For these environments the Scholte wave is dispersive with low frequencies arriving first followed by the higher frequencies. The dispersive properties of the Scholte wave can be understood qualitatively since lower frequencies have greater penetration depth into the seabed and the shear and compressional speed increases with depth. Lower frequencies will therefore excite deeper layers with higher shear and compressional wave speeds, and as a result will arrive at an earlier time.

Previous studies of Scholte wave propagation in sandy bottoms have shown the frequency content of Scholte waves to be in the range of 1-30 Hz and group speeds in the order of 100

to 400 m/s [15–18]. As these group speeds are well below the speed of sound in the water, the Scholte wave arrival follows the direct water arrival.

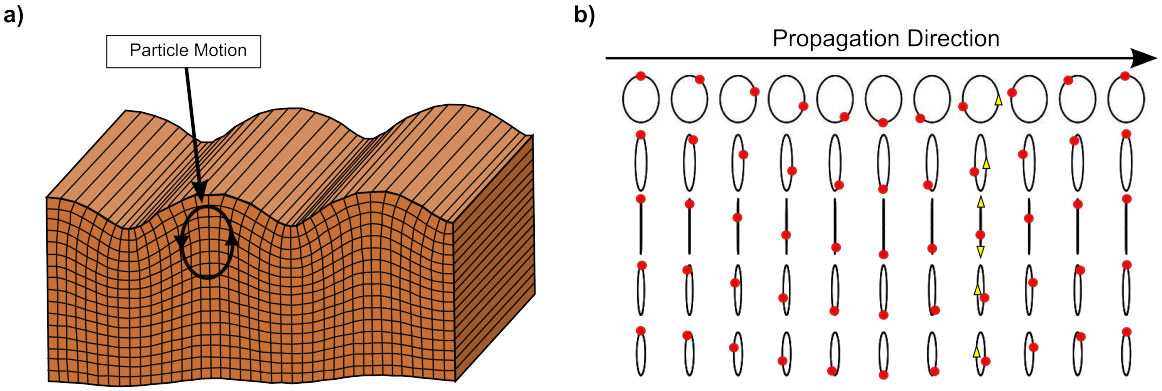

Figure 2.4: a) Surface wave displacement resulting from Scholte wave propagation and b) Particle motion of Scholte wave in sediment

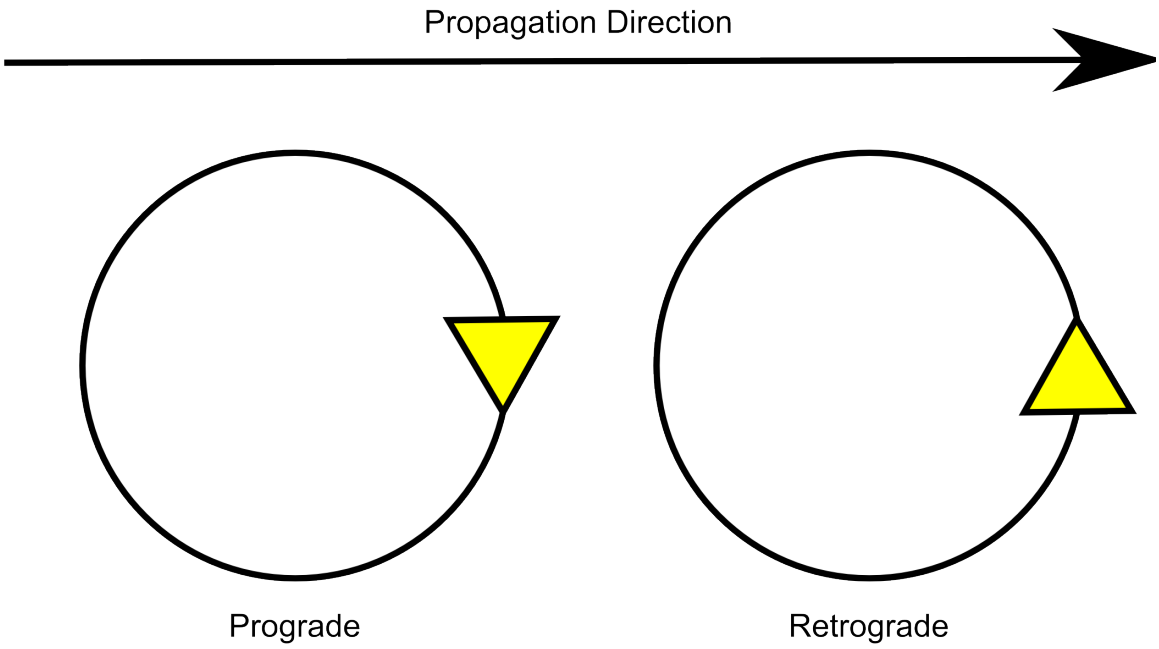

Figure 2.5: Description of prograde versus retrograde particle motion in relation to the direction of wave propagation.

Chapter 3

PEKERIS WAVEGUIDE WITH ELASTIC BOTTTOM

Valuable insight into Scholte wave propagation can be obtained from the study of simple environmental models. In this section a two layer, fluid-solid environment (referred to here as a Pekeris waveguide with an elastic bottom) will be considered using a normal mode solution. Transmission line theory will also be used as an alternate approach for deriving the characteristic equation of the waveguide. The effects of shear wave speed on transmission loss will also be investigated.

3.1 Normal Mode Equations

The two layer, fluid-solid environment that will be studied employs a cylindrical coordinate system and is shown in Figure 3.1. The environment is characterized by a homogeneous water layer with thickness h, density ρ_w, and sound speed c_w ($0 \leq Z \leq h$). The water layer is bounded above ($z \leq 0$) by a pressure release surface, and below ($z \geq h$) by an elastic-solid, isotropic, half-space with density ρ_b, compressional wave speed c_p, and shear wave speed c_s. A sinusoidal point source of frequency f (angular frequency $\omega = 2\pi f$) is located at depth $z = z_o$ and range $r = 0$.

This model was first studied by Press and Ewing [19], and later by Ellis and Chapman [20] using a normal mode solution. Using the notation from Ellis and Chapman, the normal mode equations are

$$\frac{d^2\phi_1}{dz^2} + \left(\frac{\omega^2}{c_w^2} - k_n^2\right)\phi_1(z) = 0, \qquad 0 \leq z \leq h \tag{3.1}$$

$$\frac{d^2\phi_1}{dz^2} + \left(\frac{\omega^2}{c_p^2} - k_n^2\right)\phi_1(z) = 0, \qquad z > h \tag{3.2}$$

$$\frac{d^2\phi_2}{dz^2} + \left(\frac{\omega^2}{c_s^2} - k_n^2\right)\phi_2(z) = 0, \qquad z > h \tag{3.3}$$

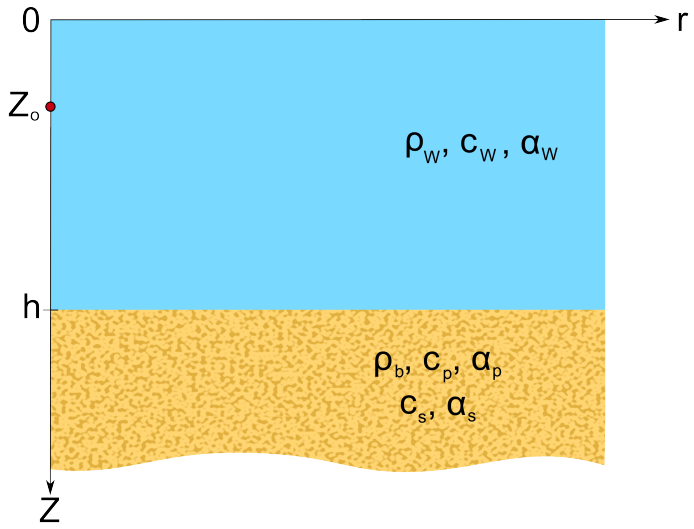

Figure 3.1: Simple two layer fluid-solid model with a homogeneous water layer that is bounded above by a pressure-release surface, and below by an elastic half-space.

where ϕ_1 and ϕ_2 are potential functions that are related to the horizontal and vertical components of particle displacement [21]. A time dependence of $e^{-i\omega t}$ and range dependence $H_o^{(1)}(k_n r)$ are assumed, where $H_o^1(k_n r)$ is the Hankel function of the first kind.

Solutions of Equations 3.1, 3.2, and 3.3 must satisfy the following conditions

- Continuity of normal stress in the z direction, τ_{zz}, at the water-sediment interface $(z = h)$.

- Continuity of shear stress parallel to the bottom, τ_{rz} at the water-sediment interface $(z = h)$. Shear stress in the water is always zero, thus at the interface the shear stress in the sediment must similarly be zero.

- Continuity of particle displacement in the z direction at the water-sediment interface $(z = h)$.

- A free surface (also referred to as a pressure release surface) at $z = 0$ where the pressure is zero.

- The Sommerfeld radiation condition must be satisfied. It requires that no energy from infinity can be radiated into a region of sources [21].

The solution for ϕ_1 and ϕ_2, are found by applying the free surface condition and the Sommerfeld radiation condition, and are given by

$$\phi_1(z) = A_n sin(\gamma_n z), \qquad 0 \leq z \leq h \tag{3.4}$$

$$\phi_1(z) = B_n e^{i\nu_n(z-h)}, \qquad z > h \tag{3.5}$$

$$\phi_2(z) = C_n e^{i\beta_n(z-h)}, \qquad z > h \tag{3.6}$$

where the vertical wave numbers are

$$\gamma_n = \left(\frac{\omega^2}{c_w^2} - k_n^2\right)^{1/2} \tag{3.7}$$

$$\nu_n = \left(\frac{\omega^2}{c_p^2} - k_n^2\right)^{1/2} \tag{3.8}$$

$$\beta_n = \left(\frac{\omega^2}{c_s^2} - k_n^2\right)^{1/2} \tag{3.9}$$

The horizontal wave numbers, k_n (for $n = 0, 1, 2, ...$) are solutions to the characteristic equation of the environment,

$$tan\,(\gamma_n h) = i\frac{\rho_b}{\rho_w}\frac{\gamma_n}{\nu_n}\left[\left(1 - \frac{2k_n^2}{k_s^2}\right)^2 + \frac{4\nu_n\beta_n k_n^2}{k_s^4}\right] \tag{3.10}$$

where $k_s = \omega/c_s$ is the shear wave number in the sediment. Equation 3.10 is found through substitution of the boundary conditions into Equations 3.4, 3.5, and 3.6.

An alternative approach for finding Equation 3.10 from Oliner [22] finds the characteristic equation through modelling the waveguide as an equivalent transmission line network where pressure is analogous to the voltage, V, and the vertical component of the particle velocity is analogous to current, I. The following sections will include a brief review of transmission line network theory, followed by the derivation of Equation 3.10 using Oliner's approach.

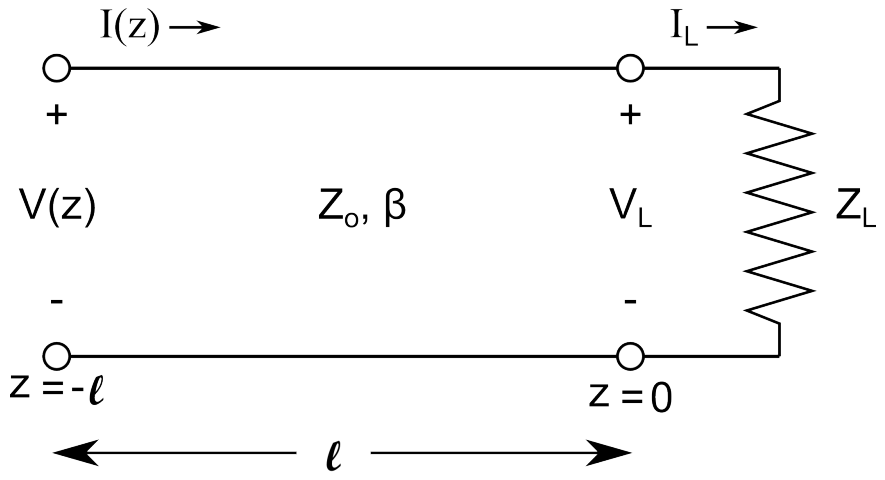

Figure 3.2: Basic transmission line of length, l, with load, Z_L,

3.2 Transmission Line Input Impedance

A key aspect of transmission line theory, as applied here, is the calculation of the input impedance, Z_{in}, of a transmission line of length, l, and characteristic impedance, Z_o, that terminated with a load, Z_L, (Figure 3.2). Here, the input impedance is nothing more than the impedance of the line seen at the point $z = -l$,

$$Z_{in} = Z(-l) = \frac{V(-l)}{I(-l)} \tag{3.11}$$

where $V(z)$ is the complex voltage and $I(z)$ is the complex current

$$V(-l) = V_o^+ \left(e^{i\beta l} + \Gamma_L e^{-i\beta l} \right) \tag{3.12}$$

$$I(-l) = \frac{V_o^+}{Z_o} \left(e^{i\beta l} - \Gamma_L e^{-i\beta l} \right) \tag{3.13}$$

with the reflection coefficient, Γ_L, given by

$$\Gamma_L = \frac{Z_L - Z_o}{Z_L + Z_o} \tag{3.14}$$

Substituting Equations 3.12, 3.13, and 3.14 into Equation 3.11, the input impedance becomes

$$\begin{aligned} Z_{in} &= Z_o \left(\frac{(Z_L + Z_o)e^{i\beta l} + (Z_L - Z_o)e^{-i\beta l}}{(Z_L + Z_o)e^{i\beta l} - (Z_L - Z_o)e^{-i\beta l}} \right) \\ &= Z_o \left(\frac{Z_L \left(e^{i\beta l} + e^{-i\beta l}\right) + Z_o \left(e^{i\beta l} - e^{-i\beta l}\right)}{Z_L \left(e^{i\beta l} + e^{-i\beta l}\right) - Z_o \left(e^{i\beta l} - e^{-i\beta l}\right)} \right) \end{aligned} \tag{3.15}$$

using the relation

$$\begin{aligned} e^{i\beta l} &= cos(\beta l) + isin(\beta l) \\ e^{-i\beta l} &= cos(\beta l) - isin(\beta l) \end{aligned} \tag{3.16}$$

Equation 3.15 reduces to

$$\begin{aligned} Z_{in} &= Z_o \left(\frac{Z_L cos(\beta l) + iZ_o sin(\beta l)}{Z_o cos(\beta l) + iZ_L sin(\beta l)} \right) \\ &= Z_o \left(\frac{Z_L + iZ_o tan(\beta l)}{Z_o + iZ_L tan(\beta l)} \right) \end{aligned} \tag{3.17}$$

Two special cases to consider are the input impedance for a short circuit and for a transmission line of infinite length. For the short circuit, where $Z_L = 0$, the input impedance from Equation 3.17 reduces to [23]

$$Z_{in} = iZ_o tan(\beta l) \tag{3.18}$$

For a transmission line of infinite length, where $\Gamma_L = 0$, Equation 3.14 gives $Z_L = Z_o$, and Z_{in} (Equation3.17) reduces to

$$Z_{in} = Z_o \tag{3.19}$$

3.3 Characteristic Equation Using Transmission Line Theory

The equivalent network representation of the Pekeris waveguide with a shear-supporting bottom is shown in Figure 3.3.

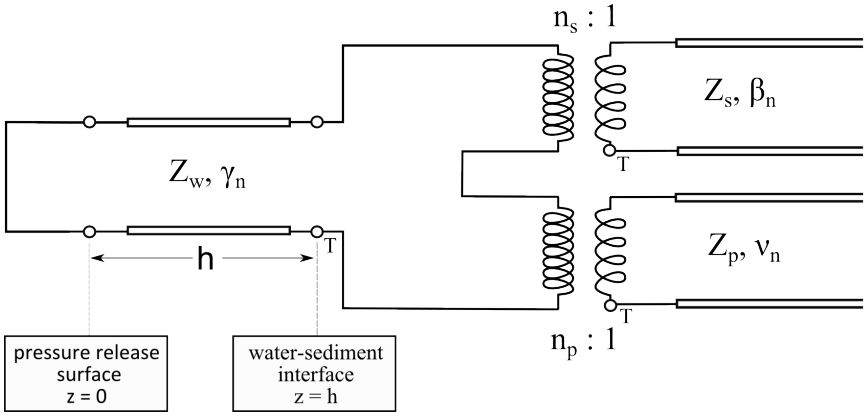

Figure 3.3: Equivalent network representation of the Pekeris waveguide with a shear supporting bottom. The turns ratio of the shear and compressional transformers are given by n_s and n_p respectively. Z_w, Z_s, and Z_p represent the characteristic impedances of the compressional wave in the water, the P wave in the sediment, and the SV wave in the sediment respectively.

In this representation, the water is modeled as a finite length transmission line of length h and characteristic impedance $Z_w = \omega/c_w$, with a short circuit representing the pressure release surface at $z = 0$. At the water-sediment interface ($z = h$), where compressional waves in the water are coupled to both compressional (P wave) and vertical shear waves (SV wave) in the sediment, the fluid-solid interface is represented by transformers with the following turns ratios

$$n_s = \frac{2k_n\beta_n}{k_s^2} \tag{3.20}$$

$$n_p = \frac{\beta_n^2 - k_n^2}{k_s^2} \tag{3.21}$$

where n_s and n_p correspond to the SV and P waves respectively. An electrical transformer is a device that transfers energy through inductance. They consist of two windings of wire, with each winding being wound a different number of times. The ratio of these windings, referred to as the turns ratio, is equivalent to the ratio of the voltages in the windings. For

the waveguide in Figure 3.1, the turns ratios quantifies how a wave in the fluid incident on the water-sediment interface is coupled to the P and SV waves in the sediment. The coupling coefficients in this waveguide will depend on the environmental parameters, and the sum of the squared coupling coefficients, $n_s^2 + n_p^2$, will always equal to 1. This reflects how energy from the incident wave in the water is transferred to the sediment and distributed betwen the P and SV waves. A full derivation of the turns ratio can be found in the Appendix of [22].

Finally, the elastic half space can be represented as infinite transmission lines; one for compressional waves with characteristic impedance $Z_p = \omega/c_p$, and a second for shear waves with characteristic impedance $Z_s = \omega/c_s$. It should be noted that shear horizontal waves (SH waves) are not included in this model as they are not coupled to the other waves in an isotropic medium.

Having defined the equivalent transmission line network for the waveguide, the characteristic equation is now found directly by using the transverse resonance relation that states that the input impedance looking both ways from some reference plane T must equal zero, or

$$\overleftarrow{Z}(T) + \overrightarrow{Z}(T) = 0 \tag{3.22}$$

Oliner explains that the Choice of T is arbitrary; here, the location of T was chosen to correspond to the water sediment interface (Figure 3.3).

The homogeneous elastic half-space is modelled as a transmission line with infinite length. From Equation 3.19, the input impedance is therefore equal to the characteristic impedance of the medium. Thus, Z_p and Z_s are

$$Z_p = \frac{\omega\rho_b}{\nu_n}, \qquad Z_s = \frac{\omega\rho_b}{\beta_n} \tag{3.23}$$

and the input impedance looking towards the sediment is

$$\overrightarrow{Z}(T) = n_p Z_p + n_s Z_s = \left(\frac{\beta_n^2 - k_n^2}{k_s^2}\right)\frac{\omega\rho_b}{\nu_n} + \left(\frac{2k_n\beta_n}{k_s^2}\right)\frac{\omega\rho_b}{\beta_n} \tag{3.24}$$

As the water column is modelled as a finite length transmission line with a short circuit at the pressure release surface, $\overleftarrow{Z}(T)$ is given by Equation 3.18

$$\overleftarrow{Z}(T) = i\left(\frac{\omega\rho_w}{\gamma_n}\right) tan(\gamma_n h) \tag{3.25}$$

Finally, from Equation 3.22 the characteristic equation for the waveguide is

$$\left(\frac{\beta_n^2 - k_n^2}{k_s^2}\right)\frac{\omega\rho_b}{\nu_n} + \left(\frac{2k_n\beta_n}{k_s^2}\right)\frac{\omega\rho_b}{\beta_n} + i\left(\frac{\omega\rho_w}{\gamma_n}\right) tan(\gamma_n h) = 0 \tag{3.26}$$

Dividing Equation 3.26 by $-i\omega\rho_f$ and re-arranging terms gives

$$tan\left(\gamma_n h\right) = i\frac{\rho_b}{\rho_w}\frac{\gamma_n}{\nu_n}\left[\left(1 - \frac{2k_n^2}{k_s^2}\right)^2 + \frac{4\nu_n\beta_n k_n^2}{k_s^4}\right] \tag{3.27}$$

which is the same as Equation 3.10.

3.4 Case Study

In this section the effect of shear speed on transmission loss will be investigated using a simple case study with a 30 Hz source and the environmental parameters from Table 3.1 in MKS units

Table 3.1: *Environmental Parameters for case study of Pekeris waveguide with elastic bottom*

c_w	1500 m/s
c_p	1800 m/s
c_s	300 and 600 m/s
ρ_w	1000 kg/m^3
ρ_b	1800 kg/m^3
h	100 m

The horizontal wavenumbers, k_n $(n = 0, 1, 2, ..)$ are found by solving Equation 3.10. Mode 0 (k_0, also referred to as the Scholte mode) is found by applying a numerical root

finding algorithm to the method described by Ellis and Chapman [20]. Muller's method has been selected as the complex root finder for it's ability to solve complex roots even when the initial input is purely real [24]. Modes n=1,2,... are found using the complex effective depth approach from Zhang and Tindle [25] that treats reflection from a homogeneous ocean bottom as being equivalent to the reflection from a pressure release surface at a depth ΔH below the true bottom.

Solutions for the horizontal wave numbers for a shear speed of 300 m/s and 600 m/s are shown in Figure 3.4 (a) and (b) respectively. It is important to note that the results discussed in this section apply to environments where $c_s < c_w < c_p$ such as sand and clay. From 3.4, the wave number corresponding to mode 0 (k_0) is purely real and is the largest wavenumber that satisfies Equation 3.10. Additionally, increasing the shear speed decreases the value of k_0.

Having found the roots to Equation 3.10, the effect of shear wave speed on transmission loss for a 30 Hz source placed at $z_o = 97$ m will be investigated for the two cases discussed previously, as well as the case where $c_s = 0$ m/s (i.e. fluid bottom) at three receiver depths; $z = 99$ m, $z = 95$ m, and $z = 85$ m (Figures 3.5-3.7 respectively). From Figure 3.5, mode 0 for $c_s = 600$ m/s has a greater influence on transmission loss than $c_s = 300$ m/s when compared to the fluid bottom case ($c_s = 0$ m/s). As the receiver depth decreases, increasing the distance between the seabed and the receiver, the effect of mode 0 decreases significantly for $c_s = 600$ m/s. For $c_s = 300$ m/s, the transmission loss is almost indistinguishable from that of the fluid bottom. If the receiver depth is decreased further, the transmission loss for $c_s = 600$ m/s will also resemble the fluid bottom case. This case study illustrates three important features on the effects of shear wave speed on transmission loss; (1) mode 0 plays a greater role in transmission loss for higher shear wave speeds, (2) mode 0 has the greatest impact for the source close to the water-sediment interface, and (3) the transmission loss begins to resembles the fluid bottom case ($c_s = 0$ m/s) as the distance between the receiver and the water-sediment interface increases. It should be noted that the effects of mode 0 on the transmission loss are most prominent for low frequencies. At higher frequencies these effects are minimal.

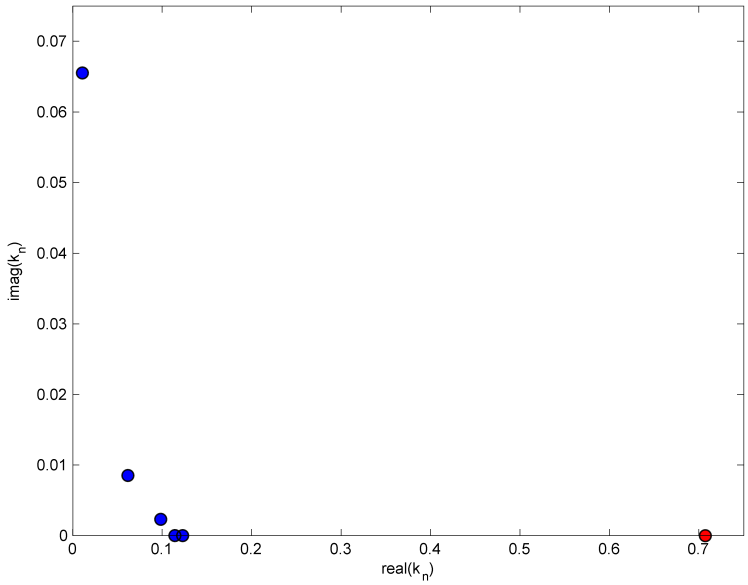

(a) $c_s = 300$ m/s

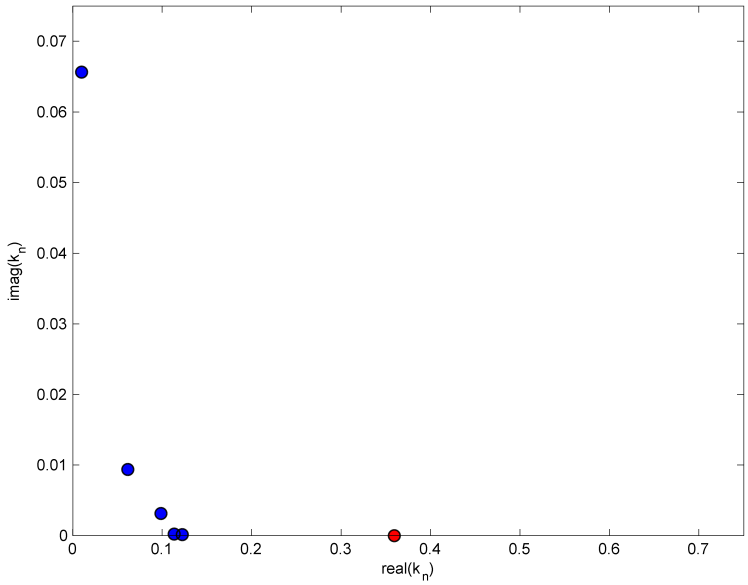

(b) $c_s = 600$ m/s

Figure 3.4: Solutions for the horizontal wave number for the environmental model described in Table 3.1. Trapped and leaky modes found using the complex effective depth approach are shown in blue, while the Mode 0 solution is shown in red.

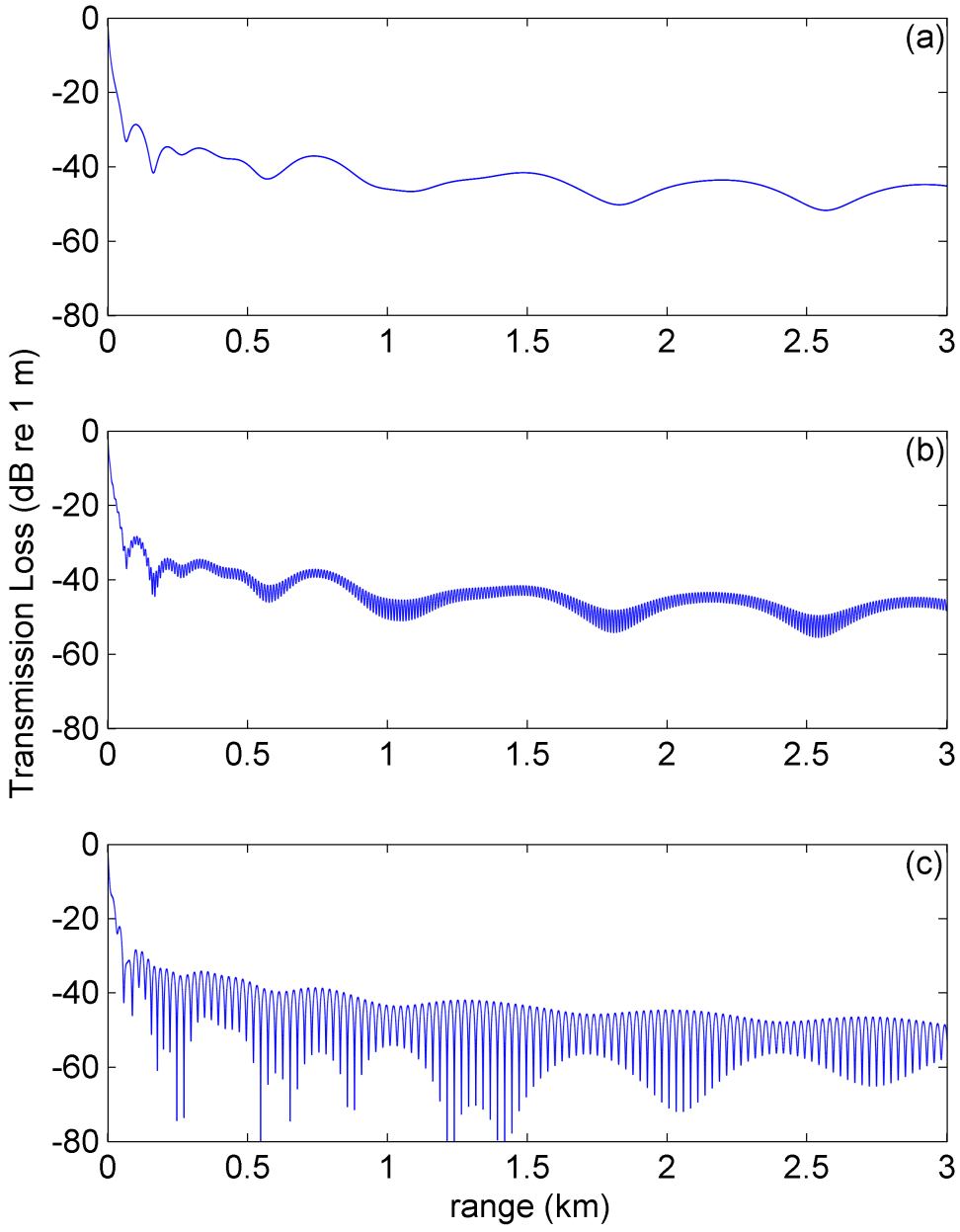

Figure 3.5: Transmission loss of 30 Hz source for receiver depth $z = 99$ m, and shear wave speed (a) $c_s = 0$ m/s, (b) $c_s = 300$ m/s, and (c) $c_s = 600$ m/s

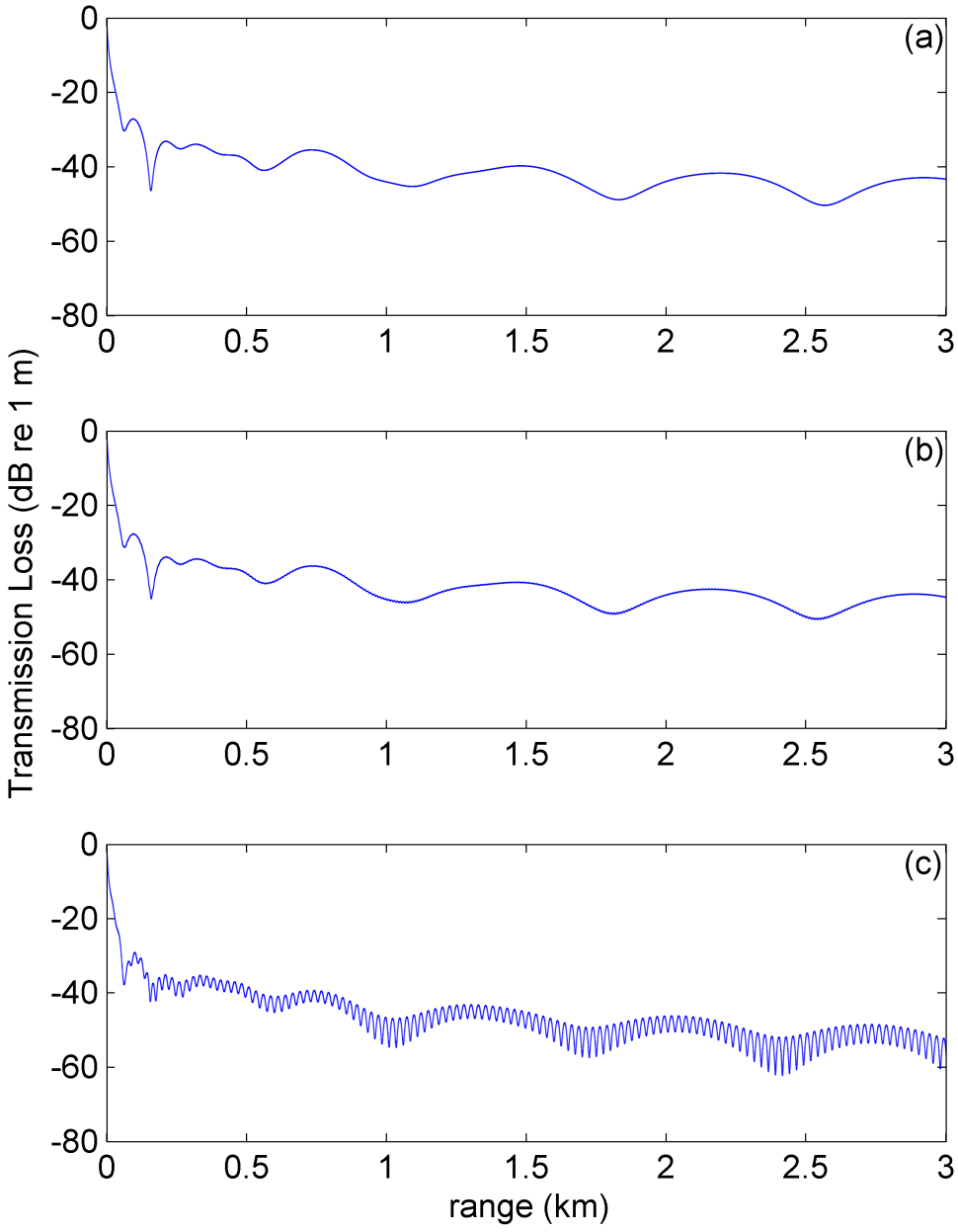

Figure 3.6: Transmission loss of 30 Hz source for receiver depth $z = 95$ m, and shear wave speed (a) $c_s = 0$ m/s, (b) $c_s = 300$ m/s, and (c) $c_s = 600$ m/s

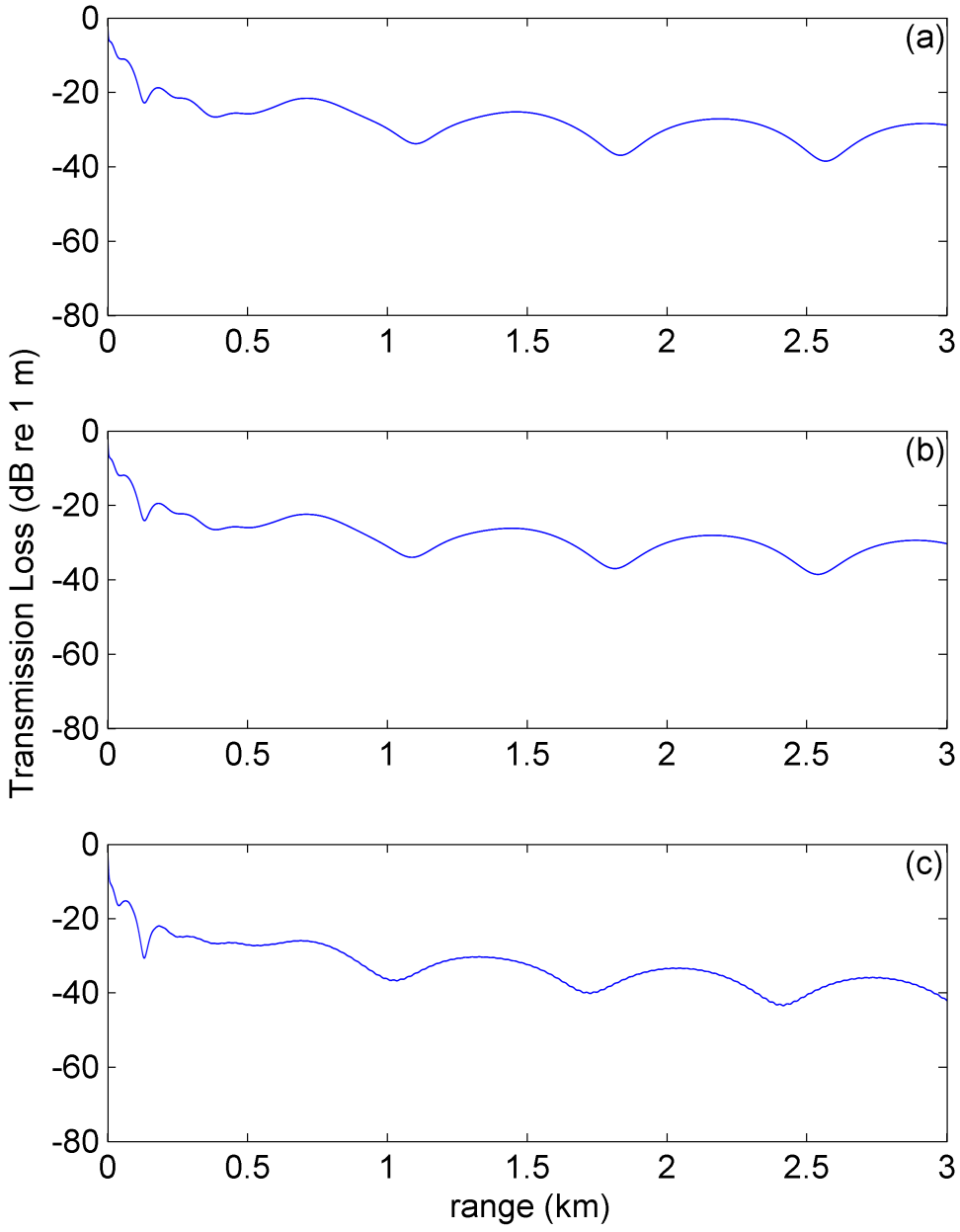

Figure 3.7: Transmission loss of 30 Hz source for receiver depth $z = 85$ m, and shear wave speed (a) $c_s = 0$ m/s, (b) $c_s = 300$ m/s, and (c) $c_s = 600$ m/s

Chapter 4
MEASUREMENT DESCRIPTION

4.1 Measurement Site

The underwater explosion measurements were conducted on 11 September 2012 at a site located approximately 7 km off the coast of Virginia Beach, Virginia. The measurement site encompasses four locations; the navy detonation site, and the mooring locations of the two measurement vessels involved, as discussed below, one of which was placed in two mooring positions over the course of the day (Figure 4.1). This area can be considered a rectangleaa of dimension 950 by 200 m that includes all four locations in Figure 4.1.

Based on existing bathymetric data from the National Oceanic and Atmospheric Administration, the mean lower low water depth of 14.3 m, where mean lower low water is defined as the average of the lower low water height of each tidal day observed over the National Tidal Datum Epoch. Tidal data for the measurement site were estimated using data from the Chesapeake Bay Bridge Tunnel tidal station (located at 36 43.2, N 76 06.84 W, 27 km from the measurement site), obtained from the National Oceanic and Atmospheric Administration Center for Operational Oceanographic Products and Services. Owing to tidal variations throughout the day (Figure 4.2), the actual water depth during the experiment varied between 14.7 and 15.0 m.

Studies in the vicinity of the measurement site, conducted by the Virginia Institute of Marine Science to determine the feasibility of sand mining [26–29], provided data on the seafloor. Data from bottom grabs and core samples from these studies show a seabed composed of unconsolidated sediments consisting of fine to course sand and clay, with significant spatial variation (Figure 4.3).

Profiles of sound speed versus depth in the water column were recorded using a YSI Castaway CTD device, which computes the sound-speed profile from direct measurements of temperature, conductivity (surrogate for salinity), and water depth. Sound-speed profiles

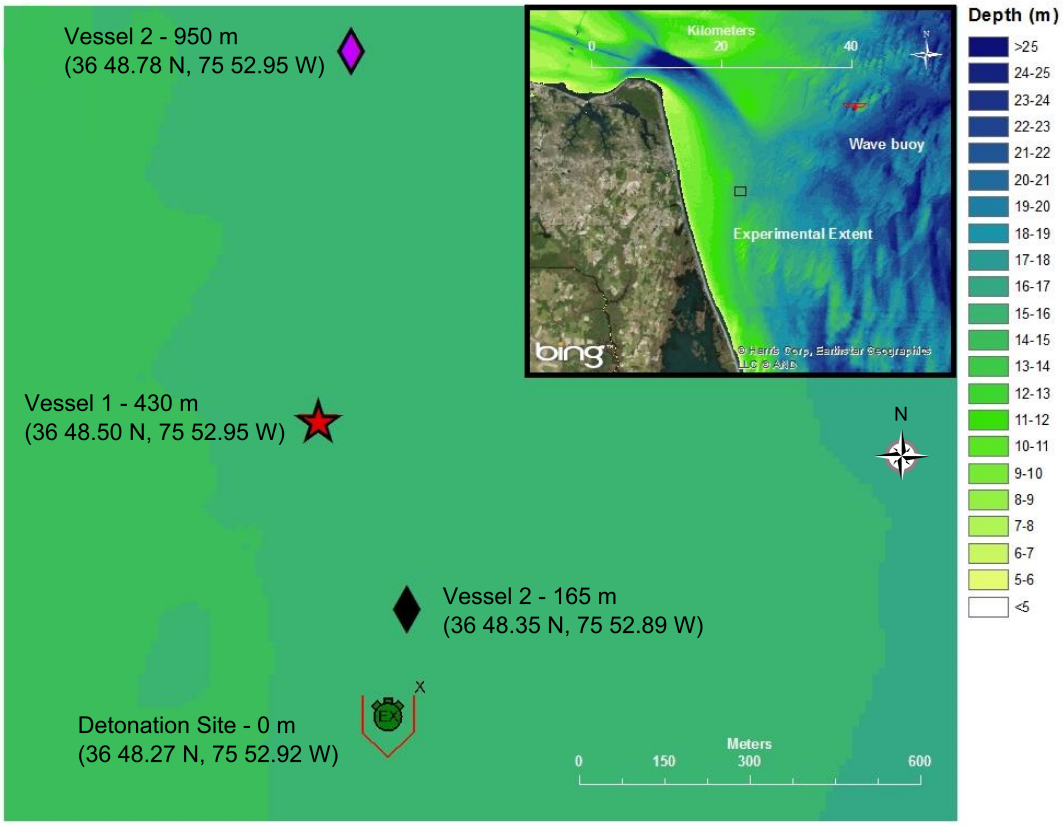

Figure 4.1: Map of measurement site with the locations of Vessel 1, Vessel 2, and the detonation site. The measurement site and wave buoy location in relation to the Virginia coastline can be found in the inset map.

were sampled at two times, 8:41:31 and 11:24:23 local time (Figure 4.4), and were found to be approximately iso-speed at 1528 m/s. Owing to significant heave motion experienced by the two research vessels, this instrument was not allowed to strike the seabed and risk damage, hence the CTD measurements do not extend to the bottom. This should not be considered an issue as the sound speed varies little with depth, particularly in the vicinity of the seabed.

During the experiment there existed a swell-wave field originating from the Northeast with this wave field not linked with local wind conditions. Sea surface wave data was ob-

tained from the National Data Buoy Centers (NDBC)Cape Henry 44099 wave buoy located at 36 54.9 N, 75 43.2 W, 19 km Northeast from the test site. During the measurement period significant wave height, defined as four times the root mean square (rms) of the wave height, varied between 1.0 m (3.3 ft) and 1.2 m (3.9 ft); alternatively the rms waveheight varied between 0.25 and 0.3 m.

4.2 Test Description

Five explosive charges were deployed as part of a training exercise for a Navy explosive ordnance disposal team. These charges had TNT equivalent weights ranging from 0.1 to 6.0 kg. Depending on test, the detonation occurred at either (approximately) 9 m depth, or on the bottom. Tests 1-4 used C-4 charges with a TNT-equivalence of 1.34 (i.e. 1 kg of C-4 produces an explosive force equivalent to 1.34 kg of TNT), while Test 5 used a CH-6 charge with a TNT-equivalence factor of 1.5. A summary of the tests is found in Table 4.1.

Table 4.1: *Test charge summary.*

Test	Local Time	Water Depth (m)	Explosive	Charge Depth	Charge Weight (kg)	TNT Equivalent	TNT Equivalent Weight (kg)
1	11:04	15.0	C-4	9 m	0.2	1.34	0.3
2	11:12	15.0	C-4	bottom	0.6	1.34	0.6
3	12:49	14.8	C-4	9 m	2.3	1.34	3
4	13:09	14.7	C-4	bottom	4.5	1.34	6
5	16:12	14.7	CH-6	9 m	0.07	1.50	0.1

4.3 Equipment and Measurement Locations

The underwater detonation site location was provided by the Navy. Measurements were made from two Vessels; the R/V Ocean Explorer (Vessel 1) located 430 m from the underwater detonation site for Tests 1-5 and the F/V Instigator (Vessel 2) located 165 m away

for Tests 1-2 and 950 m away for Tests 3-5 (Figure 4.1).

Acoustic data were recorded from Vessel 1 using a vertical line array (VLA), and a Loggerhead autonomous recording device (Figure 4.5). The VLA elements consisted of 9 hydrophones (ITC 1032) with receiving voltage sensitivity ranging from -204 to -208 dB re $V/\mu Pa$ depending on the position in the VLA. The These were spaced at 0.7 m. Data from the VLA were recorded on a multi-channel coherent data acquisition system (Astro-Med DASH-20) with each channel sampled at 62,500 Hz. The Loggerhead consisted of a single hydrophone recording at a sampling frequency of 50,000 Hz and a receiving voltage sensitivity of -220 dB re $V/\mu Pa$. The VLA and Loggerhead were attached to a weighted line secured to a davit. A HOBO data logger (HOBO), used to measure water depth, was also attached to the line and was mounted exactly half-way between Hydrophones 2 and 3. The hydrophone depths of the VLA and Loggerhead were determined using these depth measurements. A summary of the hydrophone depths can be found in Table 3.

From Vessel 2, acoustic data were using an identical Loggerhead system. Similar to the Vessel 1 setup, the Loggerhead was attached to a boat mounted line (Figure 4.5), and a HOBO data logger was used to determine the hydrophone depths (summarized in Table 4.2 and 4.3).

Table 4.2: *Depth summary of hydrophones and Hobo data loggers for Vessel 1.*

Vessel 1 Hydrophone Depths (m)					
	Test 1	Test 2	Test 3	Test 4	Test 5
Hydrophone 9	6.6	6.6	6.8	6.8	6.8
Hydrophone 8	7.3	7.3	7.5	7.5	7.5
Hydrophone 7	8.0	8.0	8.2	8.2	8.2
Hydrophone 6	8.7	8.7	8.9	8.9	8.9
Hydrophone 5	9.4	9.4	9.6	9.6	9.6
Hydrophone 4	10.1	10.1	10.3	10.3	10.3
Hydrophone 3	10.8	10.8	11.0	11.0	11.0
HOBO	11.1	11.2	11.3	11.3	11.4
Hydrophone 2	11.5	11.5	11.7	11.7	11.7
Hydrophone 1	12.2	12.2	12.4	12.4	12.4
Loggerhead	12.9	12.9	13.1	13.1	13.1

Table 4.3: *Depth summary of hydrophones and Hobo data loggers for Vessel 2.*

Vessel 2 Hydrophone Depths (m)					
	Test 1	Test 2	Test 3	Test 4	Test 5
Loggerhead	9.5	9.7	10.0	10.4	10.3
HOBO	12.1	12.3	12.7	13.0	13.0

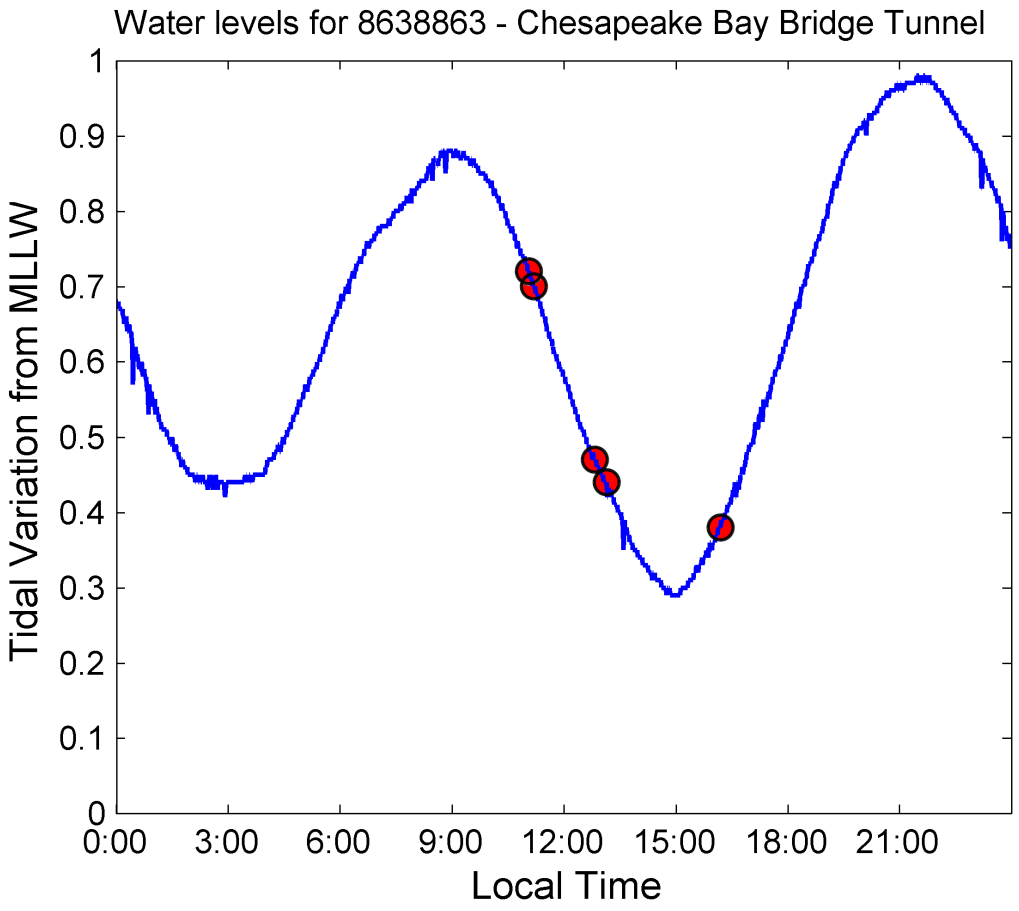

Figure 4.2: Tidal variation from Chesapeake Bay Bridge Tunnel tidal station. Height is the tidal variation in meters from the mean lower low water level. Red markers indicate underwater detonation times.

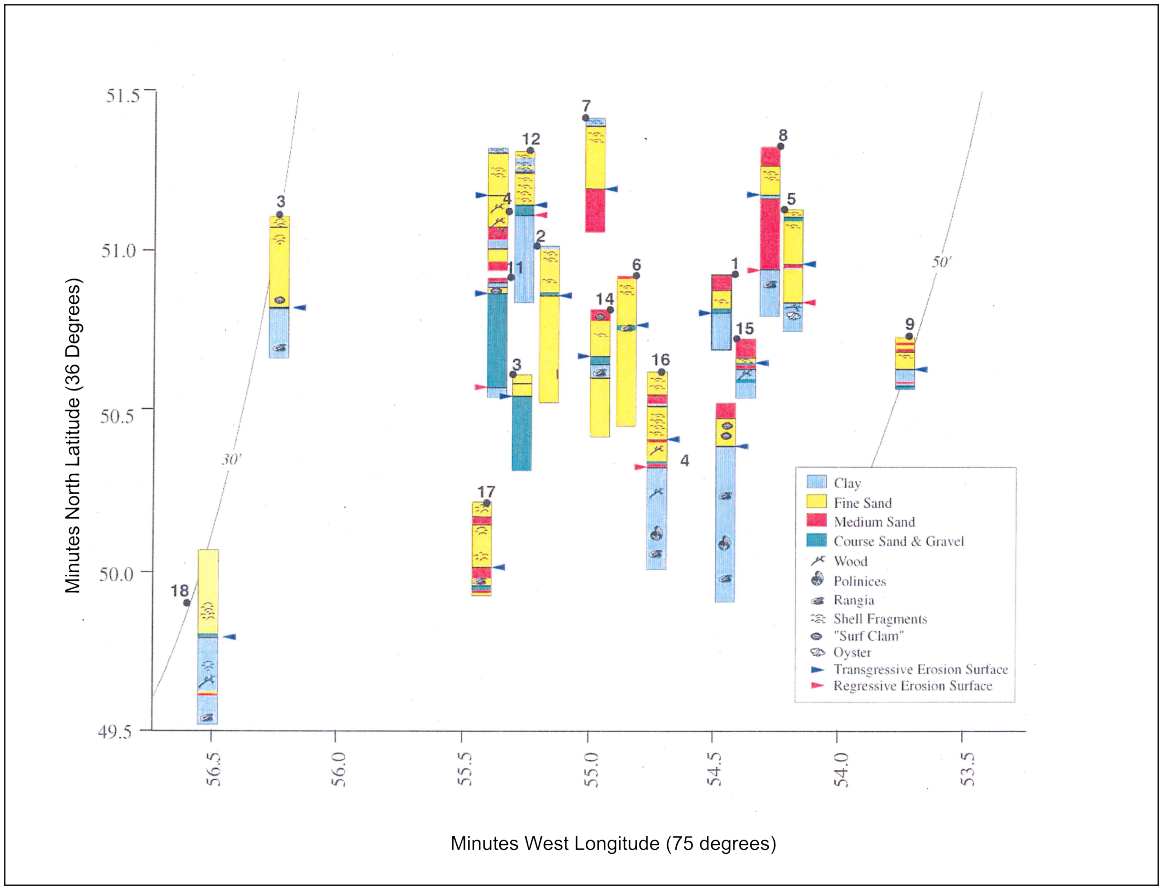

Figure 4.3: Schematic showing core samples taken from a site located 1.6 km Northwest of the measurement site. This schematic shows the composition of 18 bottom core samples (numbered 1-18 in the original report), along with 30 ft and 50 ft water depth contours. Schematic originally appeared in the report "Investigations of offshore beach sands: Virginia beach and Sandbridge, Virginia" (Reprinted with permission from Hardaway et. al. 1995)

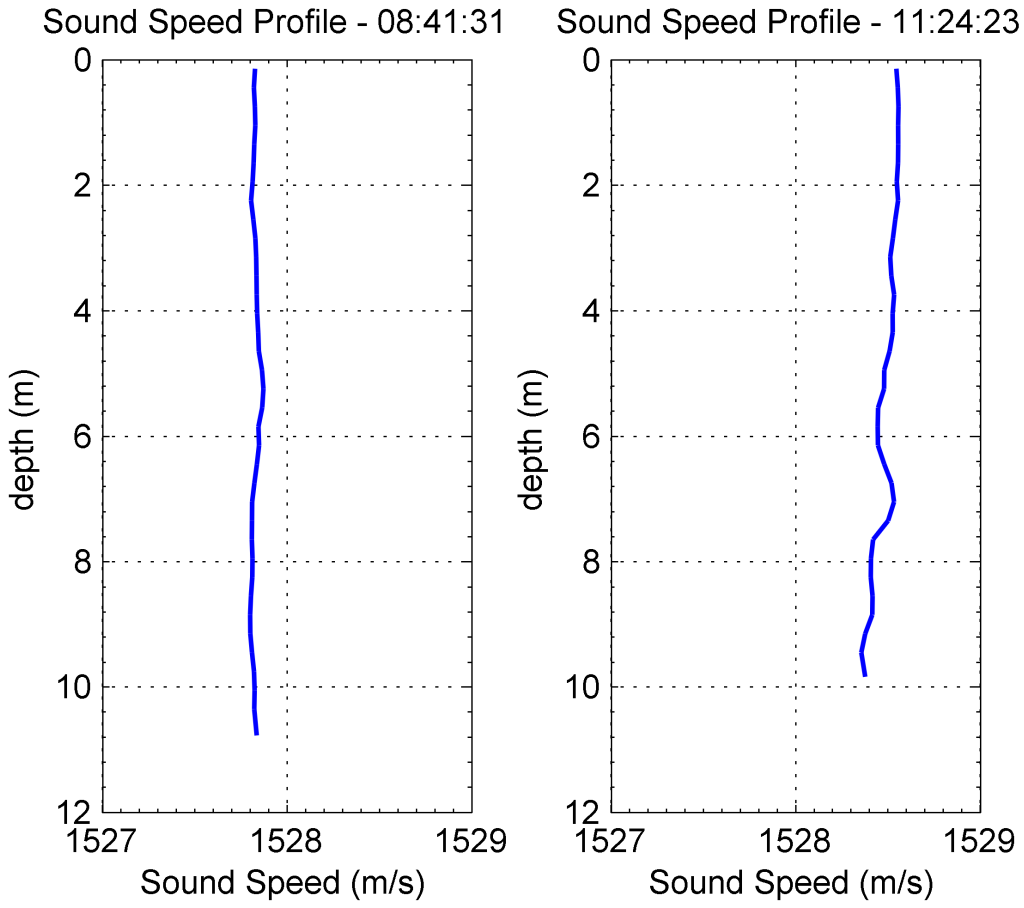

Figure 4.4: Sound-speed profiles collected using YSI CastAway CTD device. The corresponding collection times are identified.

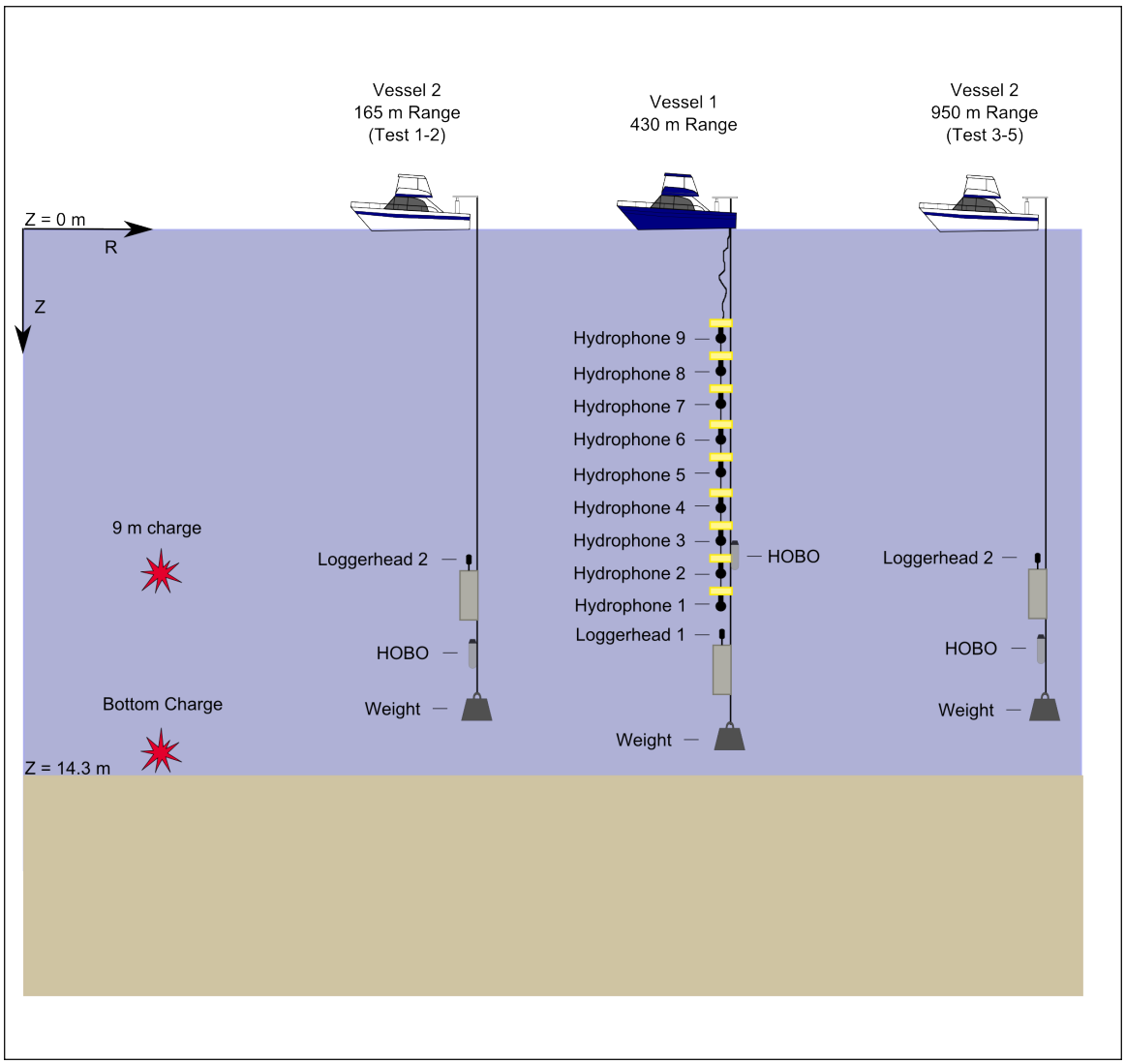

Figure 4.5: Experiment geometry for the Virginia Beach MINEX trial. A nine element VLA with hydrophones spaced 0.7 m apart and an autonomous Loggerhead system were deployed from Vessel 1. An identical loggerhead system was deployed from Vessel 2. Explosive charges were detonated at either 9 m or on the bottom of the water column. Equipment depths are listed in Table 3.

Chapter 5
RESULTS AND DISCUSSION

Results and brief discussion relating to the energy spectral density (ESD) (Section 4.1), peak pressure and bubble pulse delay measurements with comparisons to predicted values (Section 4.2), and 90% sound exposure levels (Section 4.3) for all five tests are presented. The application of the US Navy auditory weighting functions [12] to the ESD is also presented (Section 4.4). Finally, Section 4.5 gives preliminary results and discussion concerning the observation of Scholte waves in the data, the role of sediment elasticity in the generation of such waves, and related preliminary estimates of elastic parameters in the sediment. Tabulated data for this section can be found in Appendices A and B.

5.1 Energy Spectral Density and Third Octave Band

Given the transient nature of the explosion pressure signal, the spectral content of the signal is appropriately conveyed by an Energy Spectral Density (ESD). Figure 10 shows the ESD for the five tests measured from Vessel 1 on Hydrophone 1 of the VLA and Figure 11 shows the ESD simultaneously measured from Vessel 2. For each ESD, a narrow band estimate for which the frequency resolution (δf) equals 1 Hz and third-octave spectral smoothing estimate is shown.

It is readily seen that the majority of the energy is contained in the low-frequency range, approximately between 100 and 1000 Hz. Spectral interference lines revealed in the narrow band estimates (blue lines) are related to the time interference of the bubble pulses, and the overall ESD levels are highly dependent on explosive charge weight and measurement range[30] [31].

The upper frequency below which 90% of the total waveform energy is contained, identified as F_{90}, has been calculated for Tests 1-5 (Table 5.1) at the request of NAVFAC-LANT. The resulting F_{90} values are also found to be highly dependent on charge weight with F_{90}

decreasing with increasing charge weight.

Table 5.1: *Frequency below which 90% of the total waveform energy is contained*

	Test 1	**Test 2**	**Test 3**	**Test 4**	**Test 5**
F_{90} (Hz)	2518	2149	1441	978	4865

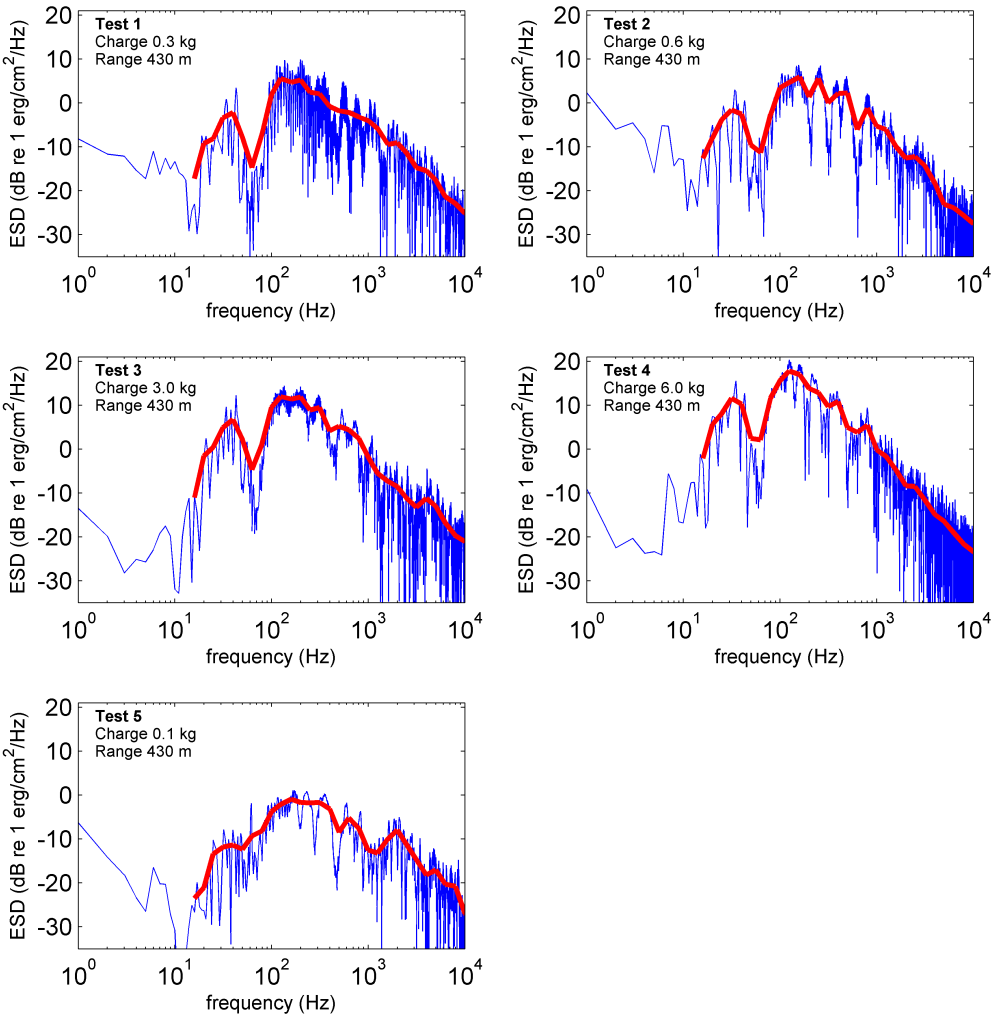

Figure 5.1: Energy spectral density (blue) and third-octave spectral smoothing (red) recorded from Vessel 1 on hydrophone 1 of the VLA. Charge weights identified in the figures represent TNT-equivalent weights.

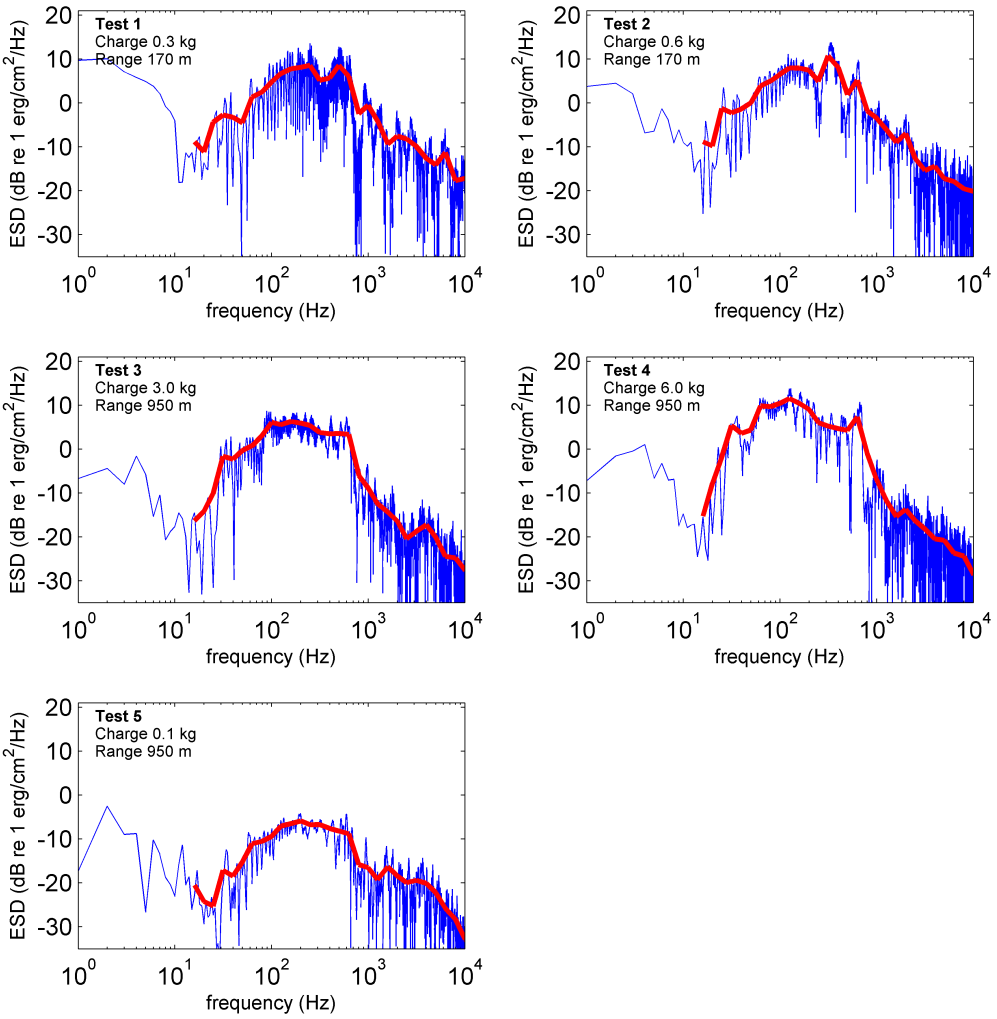

Figure 5.2: Energy spectral density (blue) and third-octave spectral smoothing (red) recorded from Vessel 2 on the Loggerhead system. Weights identified in the figures represent TNT-equivalent weights.

5.2 Comparison of Measurements to Semi-Empirical Equations

5.2.1 Peak Pressure

The peak pressure data recorded at Vessel 1 are shown with respect to depth in Figure 5.3, and show only weak variation with depth. Additionally, the Loggerhead and VLA data are in good agreement. Due to the weak depth variation, in this section the peak pressures for Vessel 1 will be presented as a single value averaged across the 9 VLA hydrophones.

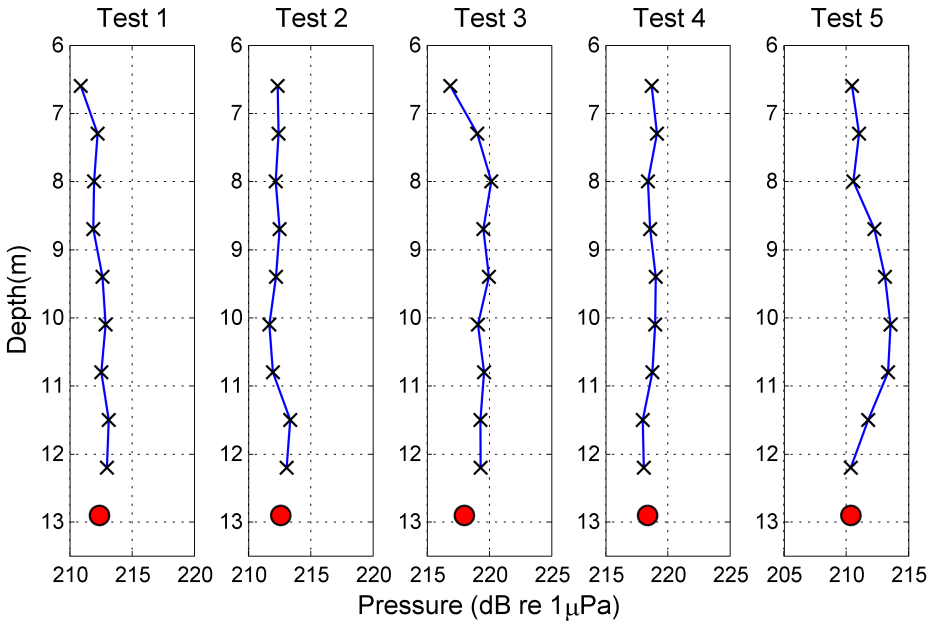

Figure 5.3: Depth dependence of the peak pressure for tests 1-5. VLA data are identified in black, and Loggerhead data are shown in red.

The peak pressures from the Vessel 1 and Vessel 2 measurements and the levels predicted by Equation 1 are plotted with respect to scaled range in Figure 5.4. A comparison of the measured and predicted levels shows reasonable agreement for the scaled-range parameter values that go from approximately 250 to 2000 $m/kg^{1/3}$. Note that there exists uncertainty in source-receiver distances for each test owing to uncertainty in vessel mooring location obtained from GPS data, and mooring watch circles that were in effect, and a nominal

uncertainty of $\pm 50m$ is estimated. From the peak pressure equation, this $\pm 50m$ uncertainty translates to ± 1 dB at the 430 m and 950 m measurement ranges, and increases to ± 5 dB for the 165 m range.

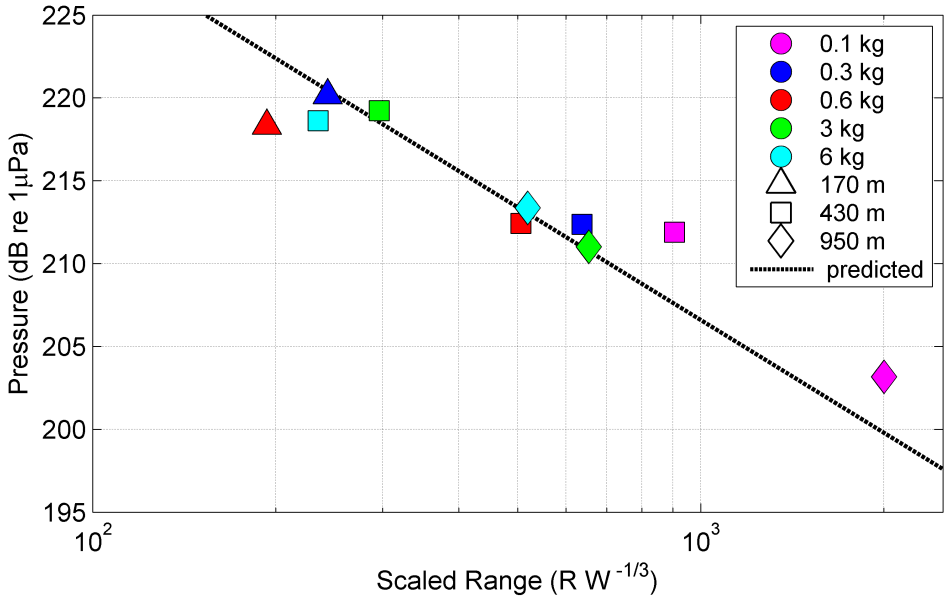

Figure 5.4: Peak pressure measurements plotted against scaled range ($RW^{-1/3}$) for Vessels 1 and 2 are shown with the predicted peak pressure from Equation 1 (black line). The marker color gives the corresponding charge weight in kg-TNT, and the marker shape identifies the measurement range.

To better illustrate how the measured data compare to predictions from Equation 2.1, results from Virginia Beach have been plotted against predicted levels along with experimental results from previous studies by Arons [3], Cole [8], and Murata et al. [6] (Figure 5.5). While the measurements from previous studies correspond to varying charge weights, explosive materials, and measurement ranges, there is good agreement between results from the various studies and the levels predicted by the peak pressure equation. For the historical data, a root-mean-squared decibel error between the data and Equation 2.1 is 1.9 dB, and for the Virginia Beach data this value is 2.4 dB.

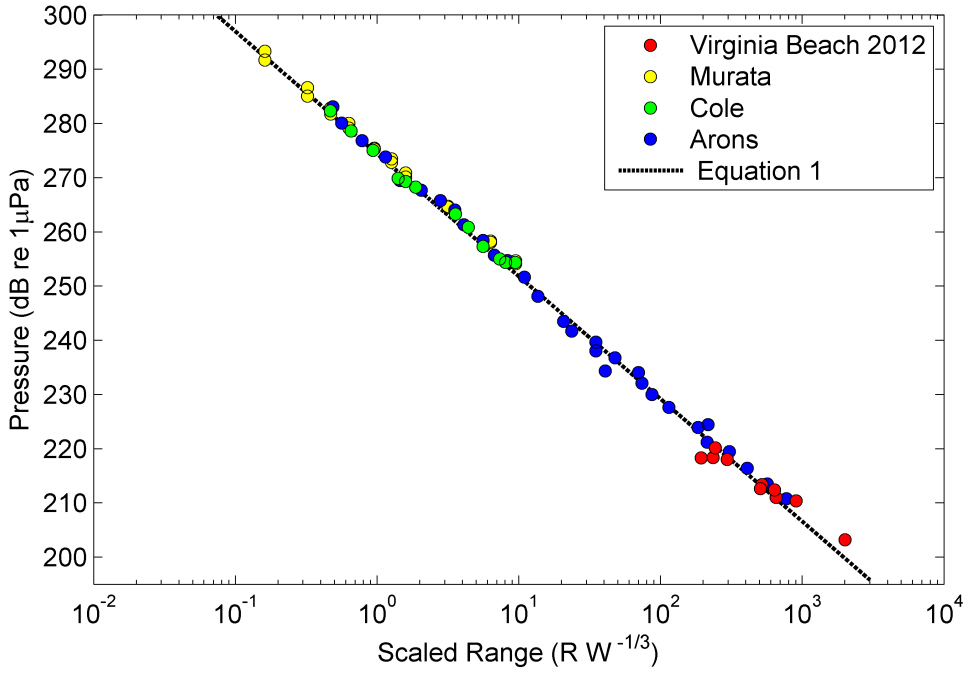

Figure 5.5: Peak Pressure from Virginia Beach MINEX trial, and previous measurements of Murata et al., Cole, and Arons are plotted against levels predicted by Equation 2.1. Historical measurements from Cole and Arons employed TNT charges, while Muratta used ammonium nitrate (0.42 TNT equivalence).

A final point of interest in the study of the peak pressure is the effect of detonation depth on the peak pressure. In Figure 5.6 the peak pressure measurements have been identified by their appropriate detonation depth (9 m or bottom). Bottom charges typically fall at or below the predicted values, while the 9 m charges are typically at or above the predicted levels.

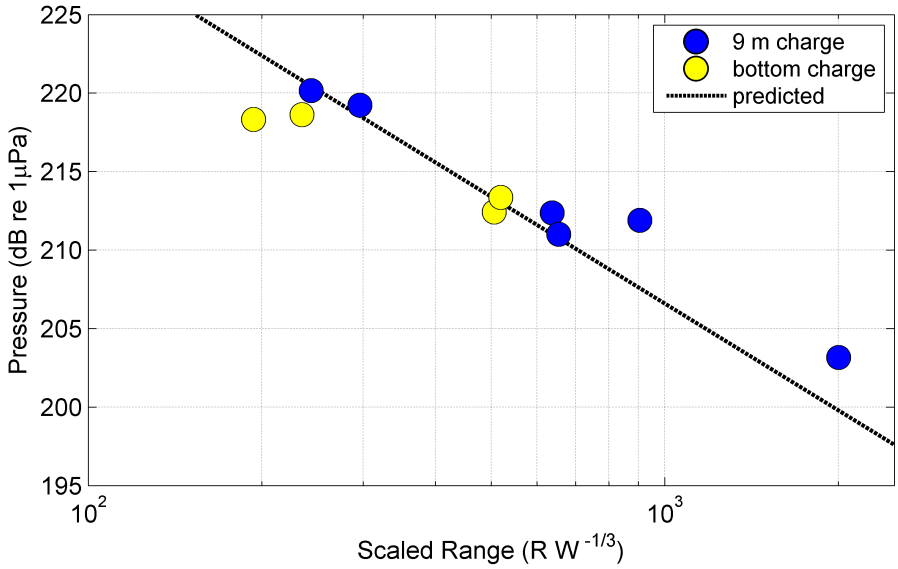

Figure 5.6: Peak pressure measurements identified by charge depth plotted against levels predicted by Equation 1

5.2.2 Sound Exposure Level

Using the SEL_{90} results from the VLA and Loggerhead at 430 m, the SEL_{90} values vary only weakly with depth, and the VLA and Loggerhead measurements are in good agreement (Figure 5.7). Given the weak depth variation, the sound exposure levels for Vessel 1 will be shown as a single value averaged across the 9 VLA hydrophones in the remainder of the results in this section. Tabulated results for SEL_{90} can be found in Appendix A, along with additional results for SEL_{100} .

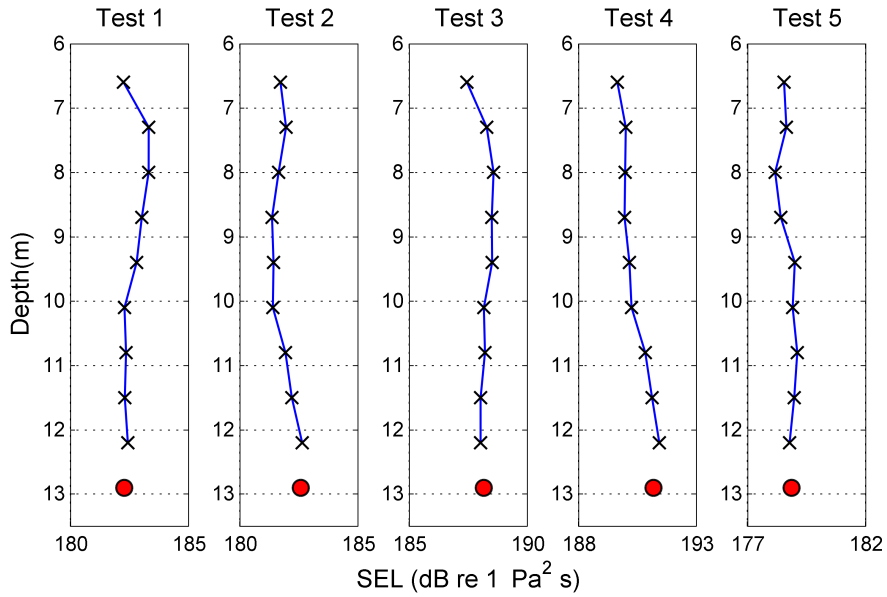

Figure 5.7: Depth dependence of SEL_{90} recorded from Vessel 1. VLA data indicated with black x, and Loggerhead data indicated by red marker.

The SEL_{90} values recorded from Vessels 1 and 2 are shown in Figure 5.8 plotted against scaled range. Unlike the peak pressure, which is dependent only on the scaled range parameter, explosive charges of different weight but at the same scaled range value can result in different SEL_{90} , with the larger charges exhibiting higher SEL_{90} levels. Our data provides only limited evidence of this, for example, as best exhibited by the two estimates made at a scaled range of approximately 500 $m/kg^{1/3}$ that differ by at least 5 dB.

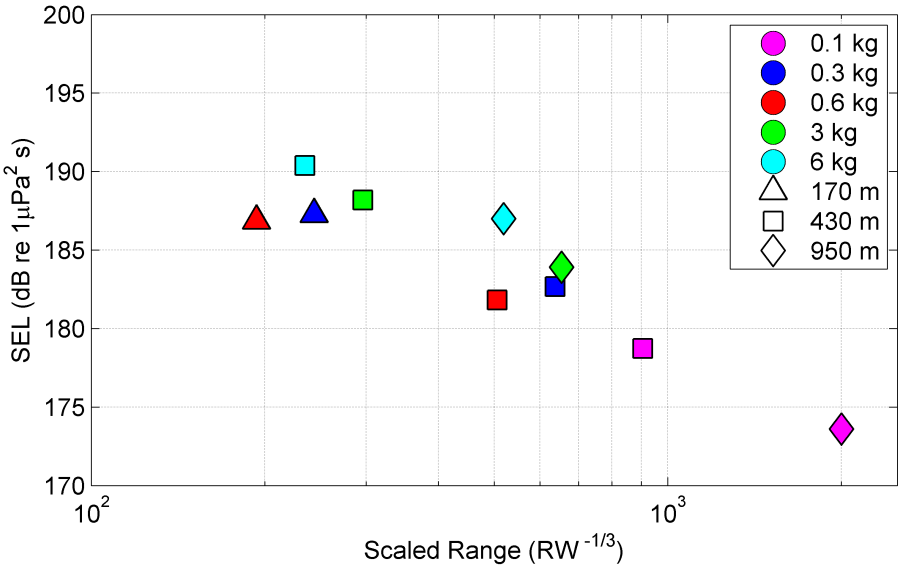

Figure 5.8: SEL_{90} for Vessels 1 and 2 plotted against scaled range ($m/kg^{1/3}$). The marker color gives the charge weight in kg-TNT, and the marker shape identifies the measurement range.

Given that SEL is a measure of the sound energy, SEL_{90} was plotted against the term $W^{1/3}\left(W^{1/3}/R\right)$ from Equation 2.9 (the semi-empirical equation for energy flux density) to determine if a simple equation for predicting SEL can be developed (Figure 5.9). With this alternate scaling approach shown on a logarithmic scale, the SEL_{90} data collapse onto a single line and exhibits a linear trend when expressed in decibels. This shows promise for the development of an empirical equation for SEL .

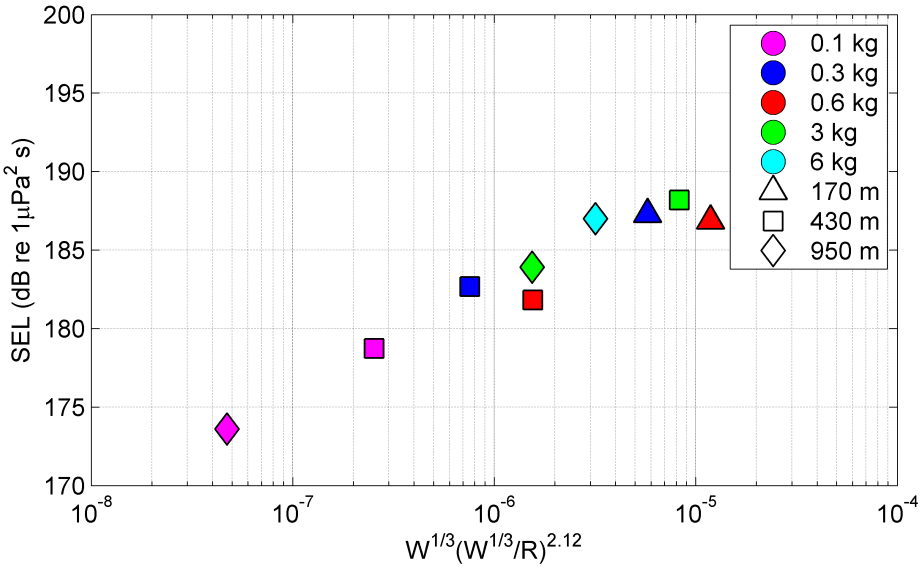

Figure 5.9: SEL_{90} for Vessels 1 and 2 plotted against range scaling from the empirical equation for energy flux density. The marker color gives the charge weight in kg-TNT, and the marker shape identifies the measurement range.

With the SEL_{90} data(in units dB re 1 $\mu Pa^2 s$) collapsing onto a line when plotted against $log_{10}\left(W^{1/3}\left(W^{1/3}/R\right)\right)$, the data was fit with a linear least squares approximation (Figure 5.10) of the form

$$SEL_{90} = m \times log_{10}\left(W^{1/3}\left(\frac{W^{1/3}}{R}\right)^{2.12}\right) + b \tag{5.1}$$

where m and b are constants. Minimizing the Euclidean 2-norm between SEL_{90} and Equation 5.1 gives the best fit to the data

$$SEL_{90} = 6.14 \times log_{10}\left(W^{1/3}\left(\frac{W^{1/3}}{R}\right)^{2.12}\right) + 219 \tag{5.2}$$

The measured SEL_{90} are shown plotted against levels predicted by Equation 5.2 (Figure 5.10). The mean-squared error between the measured and predicted SEL_{90} is ± 1.1 dB.

The SEL reported here include energy contributions from the multi-path propagation of the shock wave and from the bubble pulses. While Equation 2.9 only applies to the shock wave, Equation 5.2 is still expected to be valid since the bubble pulses do not contribute to the overall SEL.

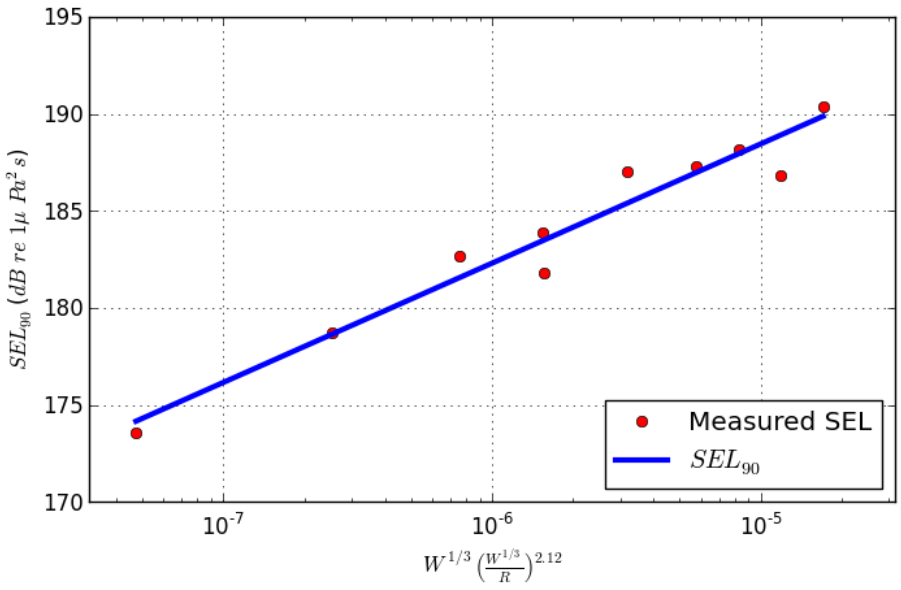

Figure 5.10: Least squares fit to SEL data plotted against the term $W^{1/3}\left(\frac{W^{1/3}}{R}\right)^{2.12}$ from Equation 2.9

The SEL data and Equation 5.2 reflect the influence of the bounded underwater waveguide. This is important as Equation 2.9 gives the energy flux density in an unbounded space where it is expected that the slope, m, from Equation 5.1 would be equal to 10 as opposed to the term 6.14 in Equation 5.2. This stems from energy conservation in a waveguide where the energy flux decreases at the rate $1/R$ which would put the slope m equal to 5.

5.3 Application of Auditory Weighting Functions

The auditory weighting functions for the functional hearing groups have been applied to the ESD for the Test 4 measurements recorded from Vessel 1 on hydrophone 1 of the VLA (Figure 5.11). As noted in Section 2.3, the auditory weighting functions emphasize ESD levels where hearing sensitivity is expected to be high, and reduces the levels where hearing sensitivity is expected to be low.

SEL are also calculated for the weighted data (See tabular results in Appendix C). While the resulting levels are highly dependent on the functional hearing group, it should be readily apparent that weighted SEL will always be less than un-weighted SEL.

While we cannot comment on the protective efficacy of auditory weighting functions we do note that their application can modify the zone of influence (ZOI) for a particular marine species. For example, weighted SEL for Mid- and High Frequency Cetaceans is expected to have a higher transmission loss than un-weighted SEL (particularly in deep water) owing to the emphasis of higher frequency content and de-emphasis of lower frequency content, and thus the ZOI will be reduced as a result of weighting.

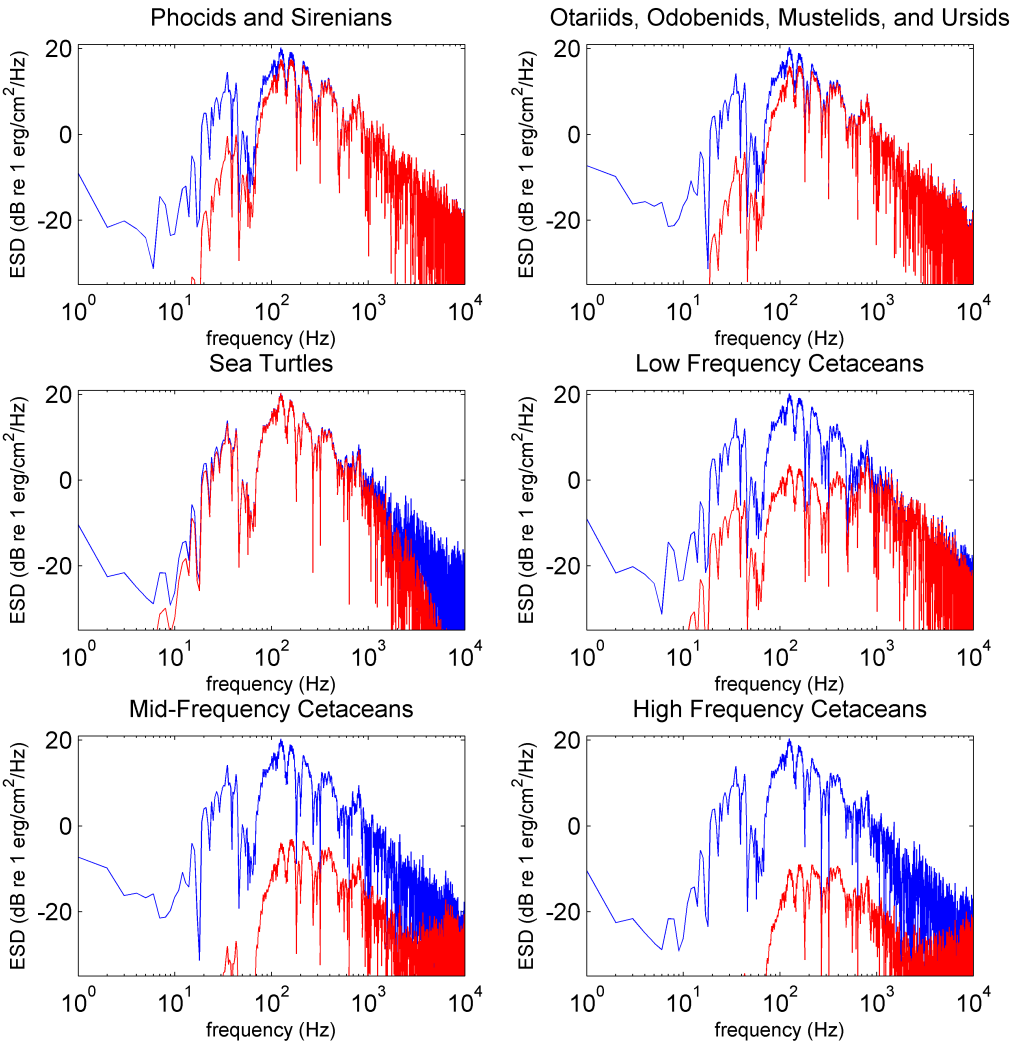

Figure 5.11: ESD for un-weighted measurement (blue) and measurements weighted by the functional hearing groups weighting function (red). ESD for Test 4 measurements recorded from Vessel 1 (range 430 m) on hydrophone 1 of the VLA.

5.4 Elastic Parameters in the Sediment

In shallow water (where there is significant interaction of sound with the water surface and ocean bottom), very low frequencies (below 50 Hz) often do not make significant contributions to the sound field. However, during the 2012 Virginia Beach measurements very low frequency measurements of order O(1-10 Hz) from Scholte waves traveling along the water-sediment interface were recorded from Vessel 1 on the VLA.

In order to successfully measure the low frequency Scholte waves, a correction was required to eliminate low-frequency roll-off on the VLA and DASH20 system. This was done by convolving the frequency-domain measurements with the reciprocal transfer function of the VLA and DASH20 (Figure 5.12). The transfer function for the equipment was calculated using manufacturers data for the impedance of the DASH20, and measured capacitance of the cables and hydrophones. It is given by

$$TF = R_{dash} + \frac{1}{i\omega C} \tag{5.3}$$

where TF is the transfer function, R_{dash} is the manufacturers specification for the resistance of the DASH20, and C is the measured capacitance of the cables and hydrophone.

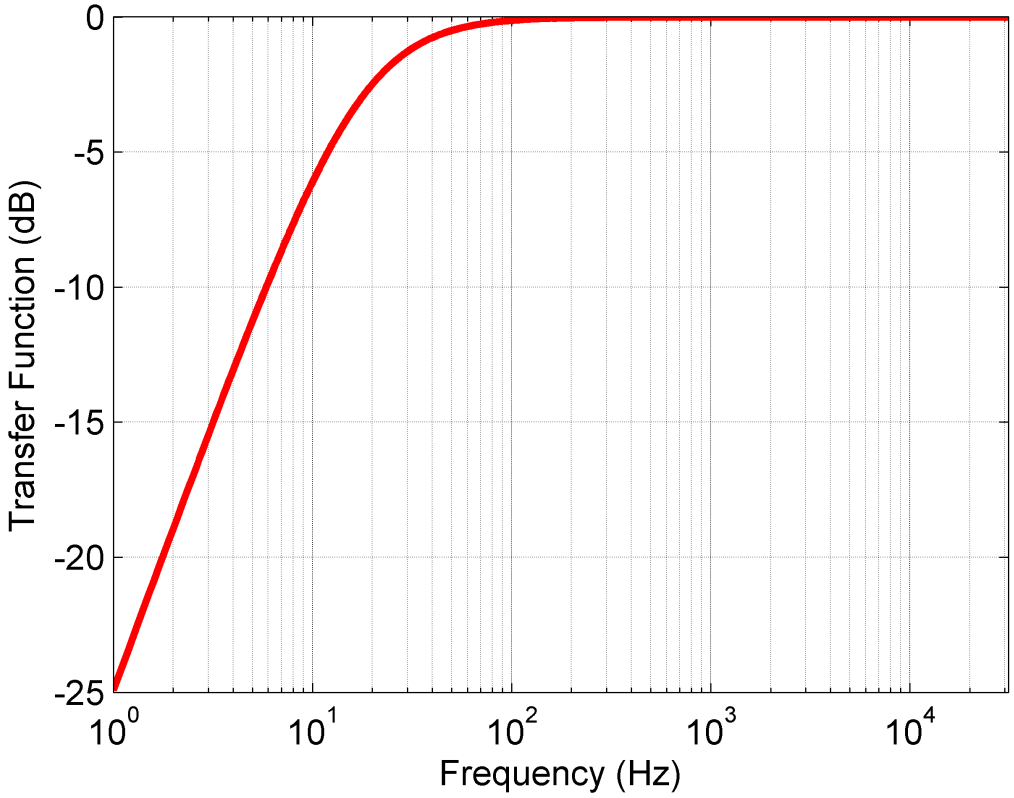

Figure 5.12: Transfer function for the VLA and DASH20 system showing the -3 dB roll-off at approximately 15 Hz.

5.4.1 Scholte Wave Time History and the Shear Speed in the Sediment

Measurements of Scholte waves were discovered in the Test 3 and Test 4 data recorded from Vessel 1 on the VLA. Time histories of the Scholte wave show arrival times between 1 s and 4 s after the direct water arrival (Figure 5.13 and Figure 5.14). Using measurements of the water sound speed (1528 m/s), the range of Vessel 1 (430 m), and knowing that the Scholte wave velocity is typically 90 - 95% of the shear speed, the shear speed in the sediment was estimated to be in the range of 100 - 370 m/s. These values are in good agreement with Hamiltons results for the shear wave velocity in sand and clay [32].

At this point the question arises as to why Scholte waves were recorded in Tests 3 and 4

but not in the other three tests. While it is difficult to give a conclusive answer to this, the likely reasons are tied to the charge weights. Tests 3 and 4 (TNT-equivalent weight 3 kg and 6 kg respectively) represent the largest charges used. As the Scholte wave experiences high attenuation rate in sand and clay sediment, these larger charges were likely able to provide sufficient energy to generate a propagating Scholte wave that could be detected by the hydrophones, while the smaller charges could not.

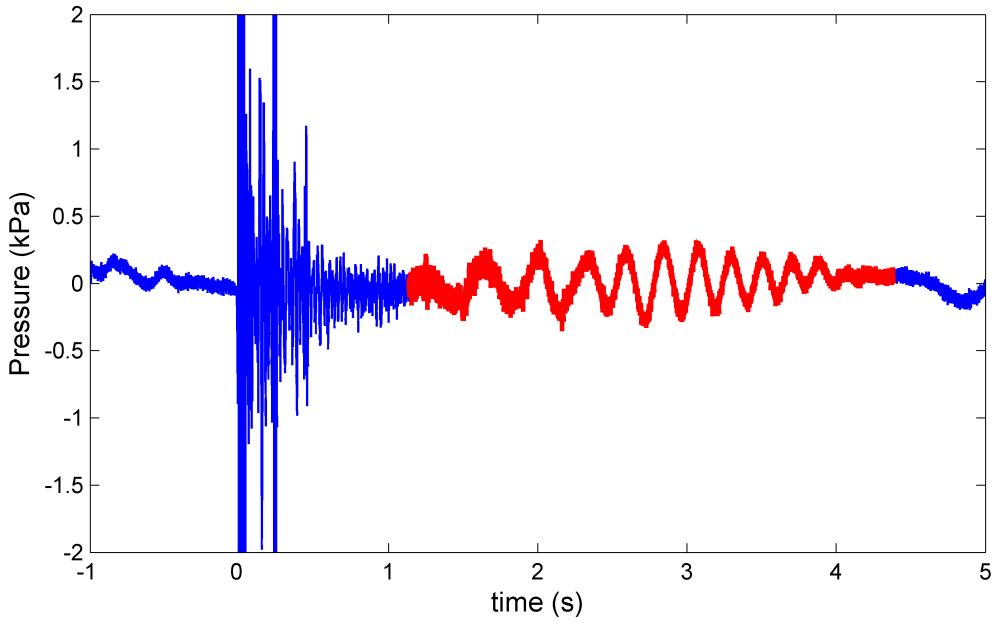

Figure 5.13: Test 3 time history with Scholte wave arrival indicated in red. The peak pressure for the shock arrival and the Scholte wave are also shown.

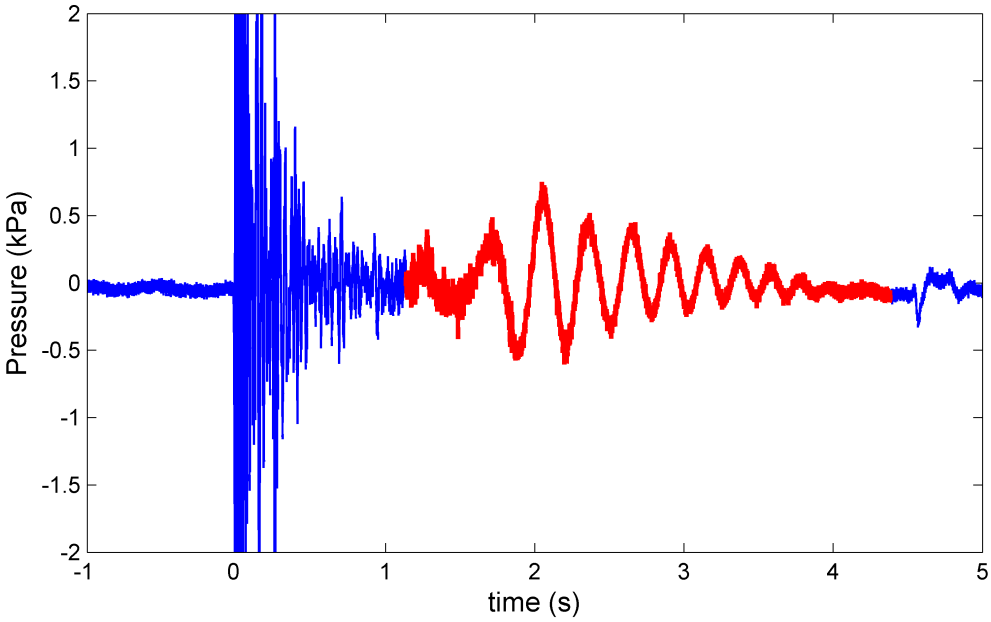

Figure 5.14: Test 4 time history with Scholte wave arrival indicated in red. The peak pressure for the shock arrival and the Scholte wave are also shown.

5.4.2 Energy Spectral Density of Scholte Wave

Most of the energy carried by the Scholte wave was in the very low-frequency range between 1 and 10 Hz for both tests (Figure 5.15 and Figure 5.16). Additionally, the deeper hydrophones (those closer to the water-sediment interface) typically measured higher levels than the more shallow hydrophones. As an example, the Test 4 ESD levels, between 1 and 6 Hz, for hydrophone 1 (nominal depth of 12.2 m) were consistently higher than levels from hydrophone 9 (nominal depth of 6.6 m). As the amplitude of the Scholte wave should decay exponentially away from the water-sediment interface, these results are expected. While the ESDs for the two tests showed some similarities, the ESD levels for Test 3 were typically lower than the Test 4 levels. Additionally, the ESD for Test 3 peaked at 4.5 Hz while Test 4 had a peak value at 3.5 Hz. Hydrophone 2 (11.7 m) has not been included due to noise present in the signal.

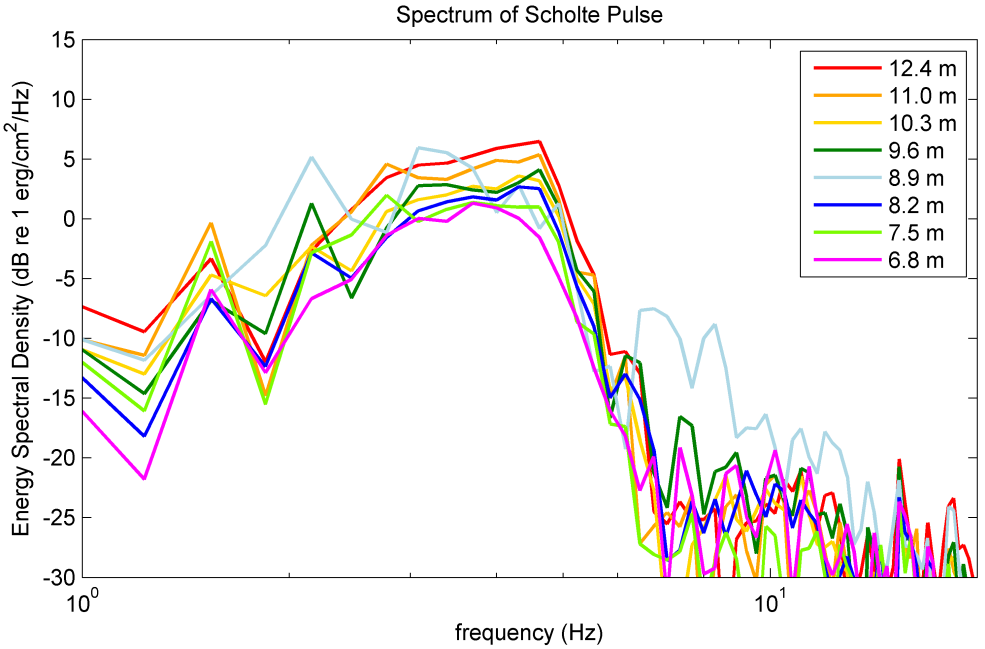

Figure 5.15: Energy spectral density of the Scholte wave recorded from Vessel 1 on the VLA during Test 3. Hydrophone 2 (11.7 m) has not been included due to noise present in the signal.

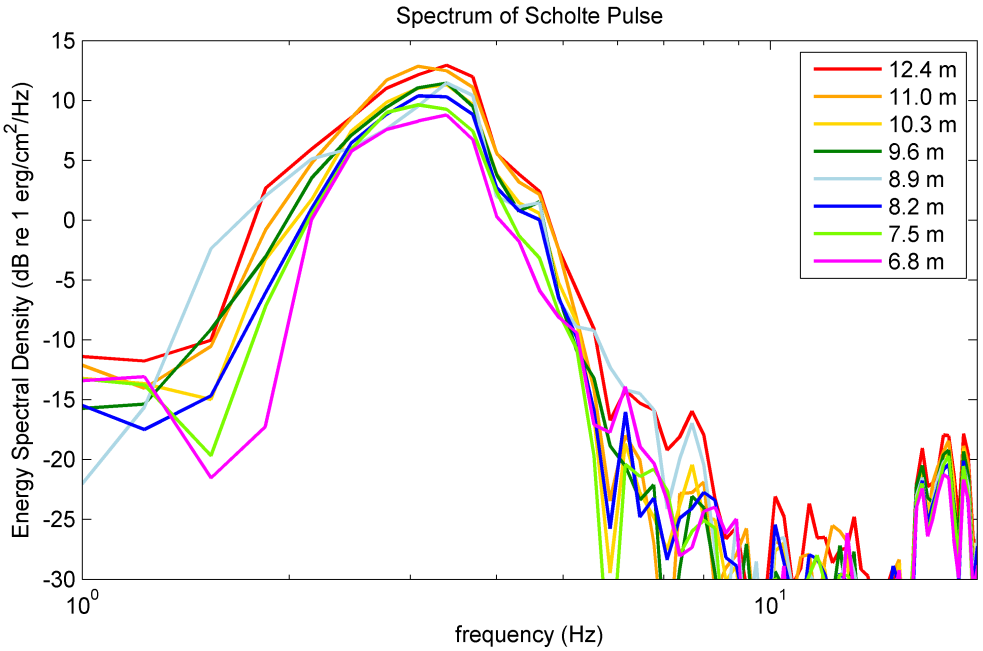

Figure 5.16: Energy spectral density of the Scholte wave recorded from Vessel 1 on the VLA during Test 4. Hydrophone 2 (11.7 m) has not been included due to noise present in the signal.

5.4.3 Time-Frequency Analysis of Scholte Wave

Time-frequency analysis of the Scholte wave data revealed dispersive characteristics, with lower frequencies (approximately 2 Hz) arriving followed by higher frequencies (approximately 5 Hz) (Figure 24 and Figure 25). The dispersive characteristics were similar for Tests 3 and 4. Interface waves in a homogenous seabed are non-dispersive [14]. Thus this dispersion reveals characteristics indicative of a complex seabed, which may include features such as layering, a sound-speed gradient, and additional attenuation due to shear. The characteristics of the dispersion are in good agreement with results from previous studies [16, 15, 17, 18].

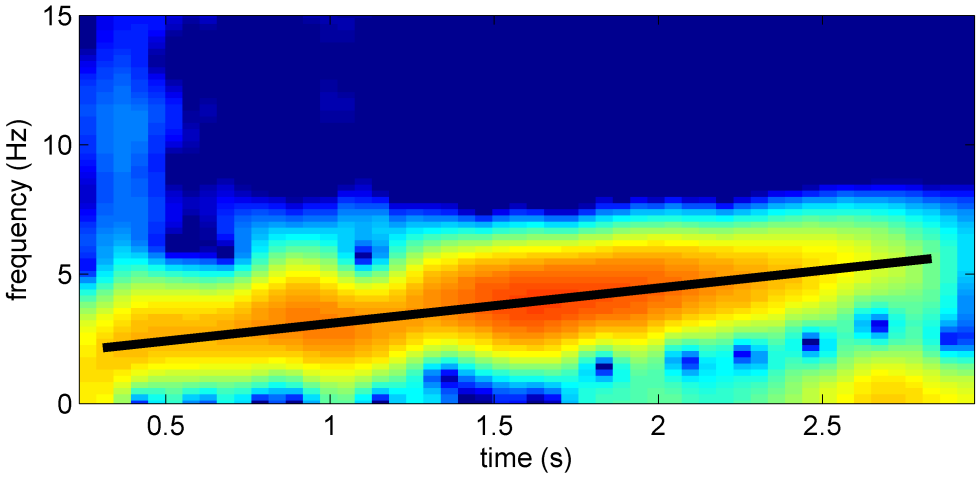

Figure 5.17: Spectrogram of the Scholte wave recorded during Test 3 from Vessel 1 on hydrophone 1 of the VLA. The black line indicates the dispersion trend.

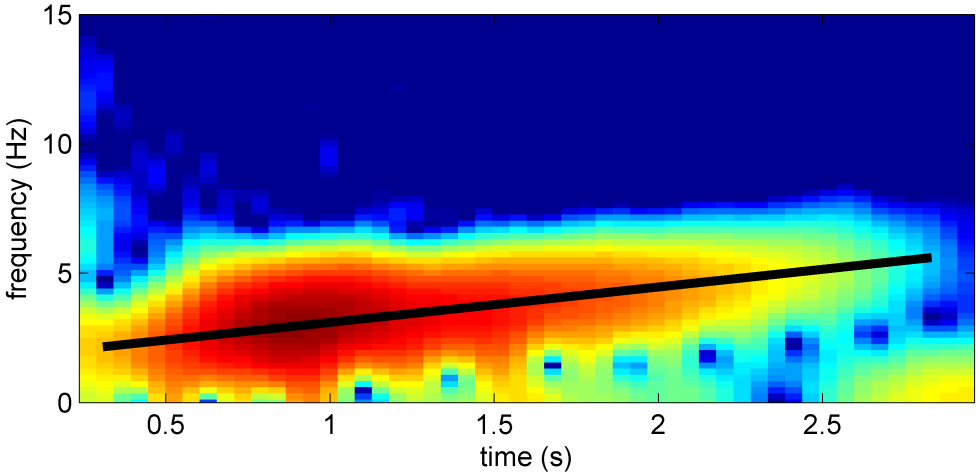

Figure 5.18: Spectrogram of the Scholte wave recorded during Test 4 from Vessel 1 on hydrophone 1 of the VLA. The black line indicates the dispersion trend.

5.5 Wavenumber Integration Modeling

To verify that the waveforms measured in Tests 3 and 4 are Scholte waves, preliminary modeling was done using the Ocean Acoustics and Seismic Exploration Synthesis (OASES) computer code [33] for modeling seismo-acoustic propagation using wavenumber integration and the Direct Global Matrix Approach [34]. Using OASES, three geo-acoustic models were used; a layered bottom that does not support shear, a single layered homogeneous bottom with constant shear speed, and a shear-supporting layered bottom. It should be noted that the purpose of this modeling was to investigate the effects of a layered bottom on the Scholte wave, and all results are preliminary at this stage. Nevertheless, the preliminary modeling results are in good agreement with our measurements insofar as they predict the observed dispersive effect.

Note that a layered bottom that does not support shear (Figure 5.19) only shows the water arrival at 0.4 s. As shear is not supported in this model, a later arrival resulting from shear in the sediment would not be expected. For the single layered homogeneous bottom with constant shear speed (Figure 5.20), the water arrival is once again visible. An additional arrival, the Scholte wave, at approximately 2 s can also be seen. As expected, this later arrival does not exhibit dispersion characteristics. Finally, in the results for a shear-supporting layered bottom (Figure 5.21) the water arrival at 0.4 s once again is present, with an additional waveform (the Scholte wave) arriving between 1.5 and 2.5 s. Unlike the Scholte wave for the homogeneous shear-supporting bottom, the characteristic Scholte wave dispersion is present in the shear-supporting, layered bottom results. These results are similar to the Scholte waves measured in Tests 3 and 4.

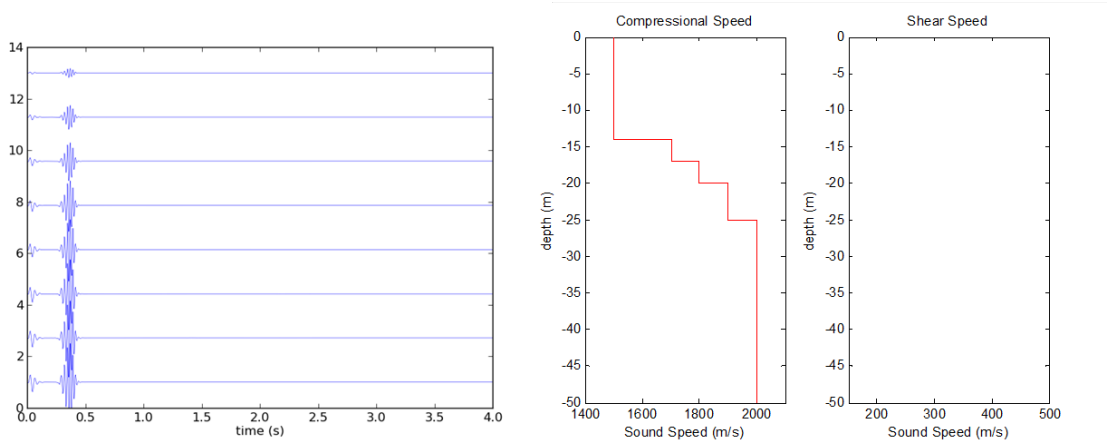

Figure 5.19: a) Results of OASES run of geo-acoustic model with layered bottom that does not support shear, and b) the corresponding compressional and shear speed in the sediment (not relevant for bottom that does not support shear). Zero water depth identifies the water-sediment interface, positive depths indicate the water, and negative depths indicate the sediment.

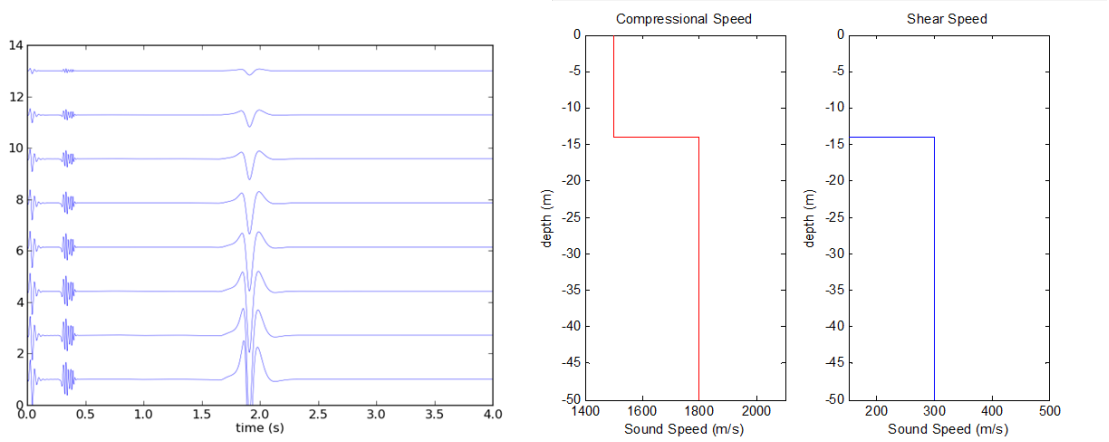

Figure 5.20: Results of OASES run of geo-acoustic model with single layer, shear-supporting, homogeneous bottom, and b) the corresponding compressional and shear speed in the sediment. Zero water depth identifies the water-sediment interface, positive depths indicate the water, and negative depths indicate the sediment.

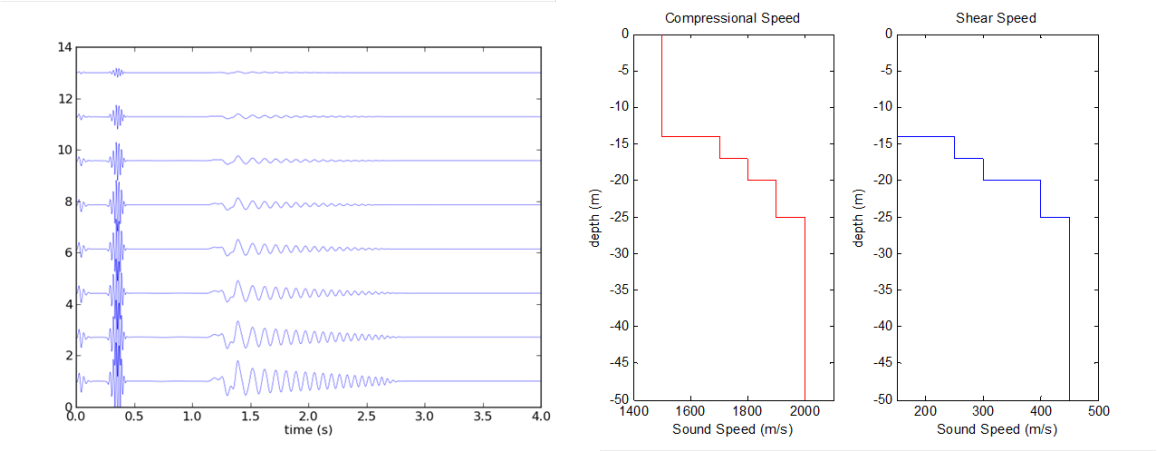

Figure 5.21: Results of OASES run of geo-acoustic model of layered, shear-supporting, homogeneous bottom, and b) the corresponding compressional and shear speed in the sediment. Zero water depth identifies the water-sediment interface, positive depths indicate the water, and negative depths indicate the sediment.

Chapter 6

SUMMARY

In September 2012 a team from the University of Washington, joined by personnel from NAVFAC-LANT, and HDR Environmental, conducted a set of measurements of the underwater sound generated by sub-surface explosions, as part of a naval training exercise. Five test charges, ranging in weight from 0.1 to 6 kg-TNT, were deployed. Measurements were collected at distances from the testing location: 165 m, 430 m, and 950 m. Acoustic data were recorded at 430 m using a vertical hydrophone array attached to a DASH20 data recorder for all five tests, and using single-element autonomous Loggerhead systems at 165 m for Tests 1 and 2 and 950 m for Tests 3-5.

Measured peak pressures and bubble pulse delays were compared to semi-empirical equations of scaled range and are in good agreement for scaled ranges 250 to 650 $m/kg^{1/3}$. For scaled ranges from 650 to 2000 $m/kg^{1/3}$ measured results varied up to 3 dB from predicted levels. Overall the measurements and predicted peak pressures were in good agreement. The bubble pulse periods for the C-4 charges (Tests 1-4) were in good agreement with the semi-empirical equation. The bubble pulse period for the CH-6 charge (Test 5), however, varied significantly from the prediction.

The measured 90% sound exposure levels ranged from 174.0 to 190.4 dB re $1\mu Pa^2s$. Unlike the peak pressure equation, various charge weights with the same scaled range did not result in the same levels. For two charges with the same scaled range, the larger charge generated a higher sound exposure level. Plotting the SEL_{90} using an alternate scaling approach borrowed from the empirical equation for the energy flux spectrum, however, shows promise for the development of an empirical equation for SEL .

Measurements of Scholte interface waves were recorded during Tests 3 and 4. The Scholte waves had arrival times between 1 and 4 s after the direct water arrival, and were of very low frequencies on the order of 1-10 Hz. Based on these arrivals, the shear speed in the sediment

was estimated to be in the range of 100 to 370 m/s. These estimates have been confirmed through preliminary modeling using the wavenumber integration approach. Additionally, time-frequency analysis of the Scholte waves revealed dispersive characteristics, where low frequencies arrive first followed later by higher frequencies.

The following are recommended areas for further research:

1. Further study on how the proximity of explosive detonation to the seabed floor, as distinct from water column, influences the peak pressure (and thus predictions peak pressure based scaled range parameter), the bubble pulse time delay (and thus predictions of explosion depth), and the generation of Scholte waves.

2. Further investigation on use of the scaling from energy flux density to develop an improved empirical equation for SEL prediction and weighted SEL prediction for use by NAVFAC and other regulatory agencies.

3. Continued investigation of Scholte waves generated by underwater explosions, and how they can be utilized to improve geo-acoustic model for a given measurement site, and thereby improve underwater sound propagation modeling. It is noted that the extremely low-frequency (less than 10 Hz) follow-on signal associated with Scholte waves can have biological implications that are neither well known nor currently addressed in auditory weighting functions.

4. Future measurements should include geophone and/or vector sensor measurements to obtain measure of acoustic particle velocity in underwater explosions.

5. Future measurements should include a portable wave buoy to investigate the effects of a rough sea surface on sound propagation.

BIBLIOGRAPHY

[1] N.R. Chapman. Measurement of the waveform parameters of shallow explosive charges. *The Journal of the Acoustical Society of America*, 78(2):672–681, 1985.

[2] John Gamble Kirkwood and William W Wood. *Shock and detonation waves.* Gordon and Breach, New York, 1968.

[3] A.B. Arons. Underwater explosion shock wave parameters at large distances from the charge. *The Journal of the Acoustical Society of America*, 26(3):343–346, 1954.

[4] R.H. Cole. *Underwater explosions.* Princeton Univ. Press, Princeton, 1948.

[5] Joseph Wakeley. Pressure-signature model for an underwater explosive charge. 27(2):445–449, 1977.

[6] Kenji Murata, Katsuhiko Takahashi, and Yulio Kato. Measurements of underwater explosion performances by pressure guage using fluoropolymer. *Journal of Material Processing Technology*, 85(1-3):09240136, 2002.

[7] Manuel E. dos Santos, Miguel N. Couchinho, Ana Rita Luis, and Emanuel J. Goncalves. Monitoring underwater explosions in the habitat of resident bottlenose dolphins. *The Journal of the Acoustical Society of America*, 128(6):3805–3808, 2010.

[8] S Temkin. A review of the propagation of pressure pulses produced by small underwater explosive charges. Memorandum NRL-MR-6181, Rutgers University, New Brunswick, NJ, 1988.

[9] John F. Slifko. Pressure-pulse characteristics of deep explosions as functions of depth and range. Technical Report NOLTR 67-87, United States Naval Ordnance Laboratory, 1967.

[10] A N Popper and M C Hastings. The effects of anthropogenic sources of sound on fishes. *Journal of fish biology*, 75(3):455–489, August 2009. PMID: 20738551.

[11] Brandon L. Southall, Ann E. Bowles, William T. Ellison, James J. Finneran, Roger L. Gentry, Charles R. Greene Jr, David Kastak, Darlene R. Ketten, James H. Miller, Paul E. Nachtigall, W. John Richardson, Jeanette A. Thomas, and Peter L. Tyack. Marine mammal noise exposure criteria: Initial scientific recommendations. *The Journal of the Acoustical Society of America*, 125(4):2517–2517, 2009.

[12] J. J. Finneran and A. K. Jenkins. Criteria and thresholds for US navy acoustic and explosive effects analysis. *SPAWAR Marine Mammal Program, San Diego, California*, 2012.

[13] Thorne Lay and Terry C Wallace. *Modern Global seismology*. Academic Press, San Diego, 1995.

[14] Dieter Rauch. Seismic interface waves in coastal waters: A review. Technical Report SR-42, SACLANTCEN, La-Spezia, Italy, November 1980.

[15] Akal and Berkson, editors. *Ocean-Seismo Acoustics*. Published in cooperation with NATO Scientific Affairs Division by Plenum Press, 1986.

[16] William A. Kuperman and Finn B. Jensen, editors. *Bottom-interacting ocean acoustics*. Published in cooperation with NATO Scientific Affairs Division by Plenum Press, New York, 1980.

[17] S. E. Dosso. Measurement of seismo-acoustic ocean-bottom properties in the high arctic. *The Journal of the Acoustical Society of America*, 98(3):1657, 1995.

[18] Guust Nolet and Leroy M. Dorman. Waveform analysis of scholte modes in ocean sediment layers. *Geophysical Journal International*, 125(2):385396, 1996.

[19] Frank Press and Maurice Ewing. Propagation of explosive sound in a liquid layer overlying a semi-infinite elastic solid. *GEOPHYSICS*, 15(3):426–446, July 1950.

[20] Dale D. Ellis and D. M. F. Chapman. A simple shallow water propagation model including shear wave effects. *The Journal of the Acoustical Society of America*, 78(6):2087–2095, 1985.

[21] W. Maurice Ewing, Wenceslas S. Jardetzky, and Frank Press. *Elastic waves in layered media*. McGraw-Hill, New York, 1957.

[22] A.A. Oliner. Microwave network methods for guided elastic waves. *IEEE Transactions on Microwave Theory and Techniques*, 17(11):812–826, November 1969.

[23] Wilbur R Le Page and Samuel Seely. *General network analysis*. McGraw-Hill, New York, 1952.

[24] William H. Press, Brian P. Flannery, Saul A. Teukolsky, and William T. Vetterling. *Numerical recipes: the art of scientific computing*. Cambridge University Press, Cambridge [England]; New York, NY, USA, 1986.

[25] Z. Y. Zhang and C. T. Tindle. Complex effective depth of the ocean bottom. *The Journal of the Acoustical Society of America*, 93(1):205–213, 1993.

[26] C.H. Hobbs III. Investigations of isolated sand shoals and associated deposits virginia inner shelf. Final contract report, Virginia Institute of Marine Science, College of William and Mary, Gloucester Point, Virginia, 1996.

[27] Suzette M. Kimball and James K. Dame. Geotechnical evaluation of sand resources on the inner shelf of southern virginia: Report & appendices a-b. Final report, College of William and Mary School of Marine Science, Virginia Institute of Marine Science, Virginia Beach, Virginia, August 1989.

[28] C. Hobbs III. *Sediments and shallow stratigraphy of a portion of the continental shelf of southeastern Virginia*. PhD thesis.

[29] C.S. Hardaway, C.H. Hobbs III, and D.A. Milligan. Investigations of offshore beach sands: Virgninia beach and sandbridge, virginia. Technical report, Virginia Institute

of Marine Science, College of William and MAry, Gloucester Point, Virginia, October 1995.

[30] D. E. Weston. Underwater explosions as acoustic sources. *Proceedings of the Physical Society*, 76(2):233, 1960.

[31] A. C. Kibblewhite and R. N. Denham. Measurements of acoustic energy from underwater explosions. *The Journal of the Acoustical Society of America*, 48:346–351, 1970.

[32] Edwin L. Hamilton. Elastic properties of marine sediments. *Journal of Geophysical Research*, 76(2):579604, 1971.

[33] Henrik Schmidt. Ocean acoustics and seismic exploration synthesis (OASES), 2012.

[34] Finn B Jensen, William A. Kuperman, Michael B. Porter, and Henrik Schmidt. *Computational ocean acoustics*. Springer, New York, NY; Heidelberg [u.a.], 2011.

Appendix A

TABULATED DATA

Table A.1: Summary of the peak pressure, bubble pulse period, SEL_{90} and SEL_{100} for Tests 1-5. Peak pressure and SEL for Vessel 1 are shown as a single averaged across the 9 VLA hydrophones.

	Peak Pressure (dB *re* $1\mu Pa$)		**Bubble Pulse Period** (s)		$\boldsymbol{SEL_{90}}$ (dB *re* $1\ \mu Pa^2 s$)		$\boldsymbol{SEL_{100}}$ (dB *re* $1\ \mu Pa^2 s$)	
Test	Vessel 1	Vessel 2	Vessel 1	Vessel 2	Vessel 1	Vessel 2	Vessel 1	Vessel 2
1	213	220	0.116	0.116	183	187	184	188
2	213	218	0.115	0.115	183	187	183	187
3	220	211	0.235	0.235	188	184	189	184
4	219	213	0.256	0.256	191	187	192	187
5	213	203	0.121	0.121	179	173	180	174

Table A.2: Depth dependence of the peak pressure as recorded from Vessel 1 on the VLA

	Peak Pressure				
	Test 1	Test 2	Test 3	Test 4	Test 5
Hydrophone 1	213	213	219	218	210
Hydrophone 2	213	213	219	218	212
Hydrophone 3	213	212	220	219	213
Hydrophone 4	213	212	219	219	214
Hydrophone 5	213	212	220	219	213
Hydrophone 6	212	213	220	219	212
Hydrophone 7	212	212	220	218	211
Hydrophone 8	212	212	219	219	211
Hydrophone 9	211	212	217	219	210
Loggerhead	212	213	218	218	210

Table A.3: Depth dependence of the SEL_{90} as recorded from Vessel 1 on the VLA

	Peak Pressure				
	Test 1	Test 2	Test 3	Test 4	Test 5
Hydrophone 1	183	183	188	192	179
Hydrophone 2	183	183	188	192	179
Hydrophone 3	183	182	189	191	180
Hydrophone 5	183	182	189	191	179
Hydrophone 6	183	182	189	190	179
Hydrophone 7	184	182	189	190	179
Hydrophone 8	184	182	189	190	179
Hydrophone 9	183	182	188	190	179
Loggerhead	183	183	188	189	179

Appendix B

NAVY EXPLOSIVES CRITERIA AND THRESHOLDS FOR MARINE MAMMALS AND SEA TURTLES

The Navy criteria and thresholds for explosives are outlined in Appendix D of The Criteria and Thresholds for U.S. Navy Acoustic and Explosive Effects Analysis [11]. The peak pressure and SEL_{90} calculated with auditory weighting functions are compared to the Navy criteria and thresholds (Figure B1 and B2). Results for SEL_{100} are also included (Figures B3 and B4).

Table B.1: Peak Pressure and SEL_{90} for Vessel 1. Levels that exceed thresholds are identified in red.

		GI Tract Injury	PTS Threshold		TTS Threshold		Behavioral Threshold
		(unweighted) Peak SPL dB re 1 µPa	SEL90 dB re 1 µPa^2 s	(unweighted) Peak SPL dB re 1 µPa	SEL90 dB re 1 µPa^2 s	(unweighted) Peak SPL dB re 1 µPa	SEL90 dB re 1 µPa^2 s
LF Cetaceans	Navy Criteria and Threshold	237	187 (Type II)	230	172 (Type II)	224	167 (Type II)
	Test 1	212	176	212	176	212	176
	Test 2	213	176	213	176	213	176
	Test 3	218	181	218	181	218	181
	Test 4	219	182	219	182	219	182
	Test 5	210	175	210	175	210	175
MF Cetaceans	Navy Criteria and Threshold	237	187 (Type II)	230	172 (Type II)	224	167 (Type II)
	Test 1	212	167	212	167	212	167
	Test 2	213	167	213	167	213	167
	Test 3	218	172	218	172	218	172
	Test 4	219	173	219	173	219	173
	Test 5	210	167	210	167	210	167
HF Cetaceans	Navy Criteria and Threshold	237	161 (Type II)	201	146 (Type II)	195	141 (Type II)
	Test 1	212	165	212	165	212	165
	Test 2	213	165	213	165	213	165
	Test 3	218	170	218	170	218	170
	Test 4	219	171	219	171	219	171
	Test 5	210	165	210	165	210	165
Phocids, Sirenians (in water)	Navy Criteria and Threshold	237	192 (Type I)	218	177 (Type I)	212	172 (Type I)
	Test 1	212	181	212	181	212	181
	Test 2	213	182	213	182	213	182
	Test 3	218	187	218	187	218	187
	Test 4	219	190	219	190	219	190
	Test 5	210	178	210	178	210	178
Otariids, Odobenids, Mustelids, Ursids	Navy Criteria and Threshold	237	215 (Type I)	218	200	212	195
	Test 1	212	181	212	181	212	181
	Test 2	213	182	213	182	213	182
	Test 3	218	187	218	187	218	187
	Test 4	219	189	219	189	219	189
	Test 5	210	178	210	178	210	178
Sea Turtles	Navy Criteria and Threshold	237	187 (Type I)	230	172 (Type I)	224	160 (Type I)
	Test 1	212	181	212	181	212	181
	Test 2	213	182	213	182	213	182
	Test 3	218	187	218	187	218	187
	Test 4	219	191	219	191	219	191
	Test 5	210	177	210	177	210	177

Table B.2: Peak Pressure and SEL_{90} for Vessel 2. Levels that exceed thresholds are identified in red.

		GI Tract Injury	PTS Threshold		TTS Threshold		Behavioral Threshold
		(unweighted) Peak SPL dB re 1 µPa	SEL90 dB re 1 µPa^2 s	(unweighted) Peak SPL dB re 1 µPa	SEL90 dB re 1 µPa^2 s	(unweighted) Peak SPL dB re 1 µPa	SEL90 dB re 1 µPa^2 s
LF Cetaceans	Navy Criteria and Threshold	237	187 (Type II)	230	172 (Type II)	224	167 (Type II)
	Test 1	220	181	220	181	220	181
	Test 2	219	179	219	179	219	179
	Test 3	211	176	211	176	211	176
	Test 4	213	178	213	178	213	178
	Test 5	203	169	203	169	203	169
MF Cetaceans	Navy Criteria and Threshold	237	187 (Type II)	230	172 (Type II)	224	167 (Type II)
	Test 1	220	173	220	173	220	173
	Test 2	219	172	219	172	219	172
	Test 3	211	167	211	167	211	167
	Test 4	213	169	213	169	213	169
	Test 5	203	160	203	160	203	160
HF Cetaceans	Navy Criteria and Threshold	237	161 (Type II)	201	146 (Type II)	195	141 (Type II)
	Test 1	220	171	220	171	220	171
	Test 2	219	170	219	170	219	170
	Test 3	211	164	211	164	211	164
	Test 4	213	165	213	165	213	165
	Test 5	203	158	203	158	203	158
Phocids, Sirenians (in water)	Navy Criteria and Threshold	237	192 (Type I)	218	177 (Type I)	212	172 (Type I)
	Test 1	220	187	220	187	220	187
	Test 2	219	186	219	186	219	186
	Test 3	211	183	211	183	211	183
	Test 4	213	186	213	186	213	186
	Test 5	203	173	203	173	203	173
Otariids, Odobenids, Mustelids, Ursids	Navy Criteria and Threshold	237	215 (Type I)	218	200	212	195
	Test 1	220	186	220	186	220	186
	Test 2	219	186	219	186	219	186
	Test 3	211	183	211	183	211	183
	Test 4	213	185	213	185	213	185
	Test 5	203	173	203	173	203	173
Sea Turtles	Navy Criteria and Threshold	237	187 (Type I)	230	172 (Type I)	224	160 (Type I)
	Test 1	220	186	220	186	220	186
	Test 2	219	186	219	186	219	186
	Test 3	211	183	211	183	211	183
	Test 4	213	187	213	187	213	187
	Test 5	203	172	203	172	203	172

Table B.3: Peak Pressure and SEL_{100} for Vessel 1. Levels that exceed thresholds are identified in red.

		GI Tract Injury	PTS Threshold		TTS Threshold		Behavioral Threshold
		(unweighted) Peak SPL dB re 1 µPa	SEL100 dB re 1 µPa^2 s	(unweighted) Peak SPL dB re 1 µPa	SEL100 dB re 1 µPa^2 s	(unweighted) Peak SPL dB re 1 µPa	SEL100 dB re 1 µPa^2 s
LF Cetaceans	Navy Criteria and Threshold	237	187 (Type II)	230	172 (Type II)	224	167 (Type II)
	Test 1	212	177	212	177	212	177
	Test 2	213	177	213	177	213	177
	Test 3	218	181	218	181	218	181
	Test 4	219	182	219	182	219	182
	Test 5	210	176	210	176	210	176
MF Cetaceans	Navy Criteria and Threshold	237	187 (Type II)	230	172 (Type II)	224	167 (Type II)
	Test 1	212	168	212	168	212	168
	Test 2	213	168	213	168	213	168
	Test 3	218	173	218	173	218	173
	Test 4	219	174	219	174	219	174
	Test 5	210	167	210	167	210	167
HF Cetaceans	Navy Criteria and Threshold	237	161 (Type II)	201	146 (Type II)	195	141 (Type II)
	Test 1	212	166	212	166	212	166
	Test 2	213	165	213	165	213	165
	Test 3	218	170	218	170	218	170
	Test 4	219	171	219	171	219	171
	Test 5	210	165	210	165	210	165
Phocids, Sirenians (in water)	Navy Criteria and Threshold	237	192 (Type I)	218	177 (Type I)	212	172 (Type I)
	Test 1	212	182	212	182	212	182
	Test 2	213	182	213	182	213	182
	Test 3	218	188	218	188	218	188
	Test 4	219	190	219	190	219	190
	Test 5	210	179	210	179	210	179
Otariids, Odobenids, Mustelids, Ursids	Navy Criteria and Threshold	237	215 (Type I)	218	200	212	195
	Test 1	212	181	212	181	212	181
	Test 2	213	182	213	182	213	182
	Test 3	218	187	218	187	218	187
	Test 4	219	190	219	190	219	190
	Test 5	210	179	210	179	210	179
Sea Turtles	Navy Criteria and Threshold	237	187 (Type I)	230	172 (Type I)	224	160 (Type I)
	Test 1	212	181	212	181	212	181
	Test 2	213	182	213	182	213	182
	Test 3	218	187	218	187	218	187
	Test 4	219	191	219	191	219	191
	Test 5	210	177	210	177	210	177

Table B.4: Peak Pressure and SEL_{100} for Vessel 2. Levels that exceed thresholds are identified in red.

		GI Tract Injury	PTS Threshold		TTS Threshold		Behavioral Threshold
		(unweighted) Peak SPL dB re 1 µPa	SEL100 dB re 1 µPa^2 s	(unweighted) Peak SPL dB re 1 µPa	SEL100 dB re 1 µPa^2 s	(unweighted) Peak SPL dB re 1 µPa	SEL100 dB re 1 µPa^2 s
LF Cetaceans	Navy Criteria and Threshold	237	187 (Type II)	230	172 (Type II)	224	167 (Type II)
	Test 1	220	182	220	182	220	182
	Test 2	219	180	219	180	219	180
	Test 3	211	176	211	176	211	176
	Test 4	213	179	213	179	213	179
	Test 5	203	170	203	170	203	170
MF Cetaceans	Navy Criteria and Threshold	237	187 (Type II)	230	172 (Type II)	224	167 (Type II)
	Test 1	220	174	220	174	220	174
	Test 2	219	173	219	173	219	173
	Test 3	211	167	211	167	211	167
	Test 4	213	169	213	169	213	169
	Test 5	203	160	203	160	203	160
HF Cetaceans	Navy Criteria and Threshold	237	161 (Type II)	201	146 (Type II)	195	141 (Type II)
	Test 1	220	172	220	172	220	172
	Test 2	219	171	219	171	219	171
	Test 3	211	164	211	164	211	164
	Test 4	213	166	213	166	213	166
	Test 5	203	158	203	158	203	158
Phocids, Sirenians (in water)	Navy Criteria and Threshold	237	192 (Type I)	218	177 (Type I)	212	172 (Type I)
	Test 1	220	187	220	187	220	187
	Test 2	219	187	219	187	219	187
	Test 3	211	183	211	183	211	183
	Test 4	213	186	213	186	213	186
	Test 5	203	174	203	174	203	174
Otariids, Odobenids, Mustelids, Ursids	Navy Criteria and Threshold	237	215 (Type I)	218	200	212	195
	Test 1	220	187	220	187	220	187
	Test 2	219	186	219	186	219	186
	Test 3	211	183	211	183	211	183
	Test 4	213	186	213	186	213	186
	Test 5	203	173	203	173	203	173
Sea Turtles	Navy Criteria and Threshold	237	187 (Type I)	230	172 (Type I)	224	160 (Type I)
	Test 1	220	186	220	186	220	186
	Test 2	219	186	219	186	219	186
	Test 3	211	184	211	184	211	184
	Test 4	213	187	213	187	213	187
	Test 5	203	172	203	172	203	172